Polarized radiative transfer, rotation measure fluctuations, and large-scale magnetic fields

Alvina Y. L. On [●],[1,2]★ Jennifer Y. H. Chan [●],[1,3,4]★ Kinwah Wu,[1,5]★ Curtis J. Saxton [●][6,7] and Lidia van Driel-Gesztelyi[1,8,9]

[1]*Mullard Space Science Laboratory, University College London, Holmbury St Mary, Surrey RH5 6NT, UK*
[2]*Institute of Astronomy, Department of Physics, National Tsing Hua University, Hsinchu 30013, Taiwan (ROC)*
[3]*Department of Physics and Astronomy, University College London, Gower Street, London WC1E 6BT, UK*
[4]*Lady Margaret Hall, University of Oxford, Norham Gardens, Oxford OX2 6QA, UK*
[5]*Perimeter Institute, 31 Caroline St N., Waterloo, ON N2L 2Y5, Canada*
[6]*Physics Department, Technion – Israel Institute of Technology, Haifa 32000, Israel*
[7]*Department of Applied Mathematics, University of Leeds, Leeds LS2 9JT, UK*
[8]*LESIA, Observatoire de Paris, Université PSL, CNRS, Sorbonne Université, Université de Paris, 5 place Jules Janssen, F-92195 Meudon, France*
[9]*Konkoly Observatory, MTA CSFK, Konkoly Thege M. út 15-17, H-1121 Budapest, Hungary*

ABSTRACT

Faraday rotation measure (RM) at radio wavelengths is commonly used to diagnose large-scale magnetic fields. It is argued that the length-scales on which magnetic fields vary in large-scale diffuse astrophysical media can be inferred from correlations in the observed RM. RM is a variable which can be derived from the polarized radiative transfer equations in restrictive conditions. This paper assesses the usage of rotation measure fluctuation (RMF) analyses for magnetic field diagnostics in the framework of polarized radiative transfer. We use models of various magnetic field configurations and electron density distributions to show how density fluctuations could affect the correlation length of the magnetic fields inferred from the conventional RMF analyses. We caution against interpretations of RMF analyses when a characteristic density is ill defined, e.g. in cases of lognormal-distributed and fractal-like density structures. As the spatial correlations are generally not the same in the line-of-sight longitudinal direction and the sky plane direction, one also needs to clarify the context of RMF when inferring from observational data. In complex situations, a covariant polarized radiative transfer calculation is essential to capture all aspects of radiative and transport processes, which would otherwise ambiguate the interpretations of magnetism in galaxy clusters and larger scale cosmological structures.

Key words: magnetic fields – polarization – radiation mechanisms: non-thermal – radiative transfer – galaxies: clusters: intracluster medium – large-scale structure of Universe.

1 INTRODUCTION

Magnetic fields are present at all scales throughout the Universe, from stars and substellar objects to galaxies, groups, clusters, and large-scale structures such as filaments and voids (see e.g. Widrow 2002; Widrow et al. 2012, for reviews). Stellar magnetic fields can be determined spectroscopically, e.g. by measuring Zeeman splitting in the optical spectral lines for low-mass solar-like stars and magnetic white dwarfs (e.g. Wickramasinghe & Ferrario 2000; Reiners et al. 2013), from separations or locations of the cyclotron harmonic features in the optical/infrared spectra for accreting white dwarfs (e.g. Wickramasinghe & Meggitt 1985; Wu & Wickramasinghe 1990), and from the X-ray spectra of neutron stars (e.g. Nagase et al. 1991; Santangelo et al. 1999; Staubert et al. 2019). Determination of magnetic field properties in larger astrophysical systems is less direct. For magnetic fields in diffuse astrophysical systems, such as the interstellar medium (ISM), intracluster medium (ICM), and intergalactic medium (IGM), their properties are often inferred from the polarized radiation traversing and/or emitted from the media. Faraday rotation measure (RM)[1] has been identified

---

★ E-mail: alvina.on.09@ucl.ac.uk (AYLO); y.chan.12@ucl.ac.uk (JYHC); kinwah.wu@ucl.ac.uk (KW)

[1] 'Faraday depth' and 'rotation measure' can only be used interchangeably in the case of a single point source along the line of sight.

as a diagnostic tool for magnetic fields in our Galaxy (see e.g. Simard-Normandin & Kronberg 1980; Han, Manchester & Qiao 1999; Brown, Taylor & Jackel 2003; Gaensler, Beck & Feretti 2004; Brown et al. 2007; Haverkorn et al. 2008; Oppermann et al. 2012; Han et al. 2015; Han 2017), nearby galaxies (e.g. Gaensler et al. 2005; Beck 2009; Mao et al. 2010, 2017), and also some galaxy clusters (e.g. Carilli & Taylor 2002; Vogt & Enßlin 2003; Clarke 2004; Govoni & Feretti 2004; Brentjens & de Bruyn 2005; Bonafede et al. 2010; Kuchar & Enßlin 2011; Vacca et al. 2018).

Recently, there have also been studies utilizing the Faraday rotation of distant polarized radio sources such as quasars (e.g. Kronberg et al. 2008; Xu & Han 2014b) and fast radio bursts (FRBs) (e.g. Xu & Han 2014a; Zheng et al. 2014; Akahori, Ryu & Gaensler 2016; Ravi et al. 2016; Vazza et al. 2018; Hackstein et al. 2019), as a means to detect and probe cosmological magnetic fields. These fields, permeating the cosmic web of filaments and voids, are weak, and their properties are often inferred statistically (e.g. Akahori, Gaensler & Ryu 2014; Vernstrom et al. 2019), or indirectly constrained through the non-detection of GeV gamma rays (e.g. Neronov & Vovk 2010; Dermer et al. 2011; Taylor, Vovk & Neronov 2011; Takahashi et al. 2013).

The statistical characterization of cosmological magnetic fields can be improved with a denser all-sky RM grid from the Square Kilometre Array (SKA), including its pathfinders, the Low-Frequency Array (LOFAR), the Murchison Widefield Array (MWA), the Expanded Very Large Array (EVLA), and its precursors, the Australian SKA Pathfinder (ASKAP) and MeerKAT (see e.g. Gaensler et al. 2010; Beck 2015; Johnston-Hollitt et al. 2015). How to properly characterize magnetic fields beyond the scale of galaxy clusters is a challenge in theoretical and observational astrophysics.

Faraday rotation measure fluctuation (RMF) analysis is proposed as a means to probe the structures of large-scale magnetic fields (e.g. Akahori & Ryu 2010; Beck et al. 2013). RM and RMF analyses are essentially based on the theory of polarized radiative transfer under certain restricted conditions. It is therefore important to have a proper understanding of the information we extract from the analyses and under what conditions the analyses enable unambiguous interpretations.

In this paper, we examine the RMF analyses in the context of polarized radiative transfer. We clarify the conditions under which the RMF method will give meaningful inferences and identify the circumstances where we should be cautious when applying the method. We organize the paper as follows. In Section 2, we present the formal covariant polarized radiative transfer formulation and show how it reduces to the standard RM under certain conditions. In Section 3, we examine the RMF analysis in the context of polarized radiative transfer. We also identify the mathematical and statistical properties of the analyses. In Section 4, we construct model density and magnetic field structures and use them to test the validity of the RMF analyses. We also discuss their astrophysical implications. In Section 5, we present our findings and warnings. Unless otherwise stated, this work uses c.g.s. Gaussian units.

2 POLARIZED RADIATIVE TRANSFER

2.1 Covariant transport in Stokes-parameter representation

Under the conservation of photon number and the conservation of phase-space volume (see Fuerst & Wu 2004; Younsi, Wu & Fuerst 2012), the covariant polarized radiative transfer equation may be expressed as

$$\frac{d\mathcal{I}_i}{d\lambda_a} = -k_\alpha u^\alpha \Big|_{\lambda_{a,co}} \left\{ -\kappa_{ij,co} \left(\frac{I_j}{\nu_{co}^3} \right) + \frac{\epsilon_{i,co}}{\nu_{co}^3} \right\} \tag{1}$$

(see Chan et al. 2019). Here, ν is the radiation frequency, $\mathcal{I}_i$ is the Lorentz-invariant Stokes vector, λ_a is the affine parameter, and $-k_\alpha u^\alpha \big|_{\lambda_{a,co}}$ is the projection factor for a photon with a four-momentum k^α travelling in a fluid with a four-velocity u^β. The subscript 'co' denotes that the quantity is evaluated in the reference frame co-moving with the fluid. The transfer matrix, $\kappa_{ij,\,co}$, accounts for the absorption and Faraday propagation effects, while the emission coefficients are defined by $\epsilon_{i,\,co}$.

In a Friedmann–Robertson–Walker (FRW) universe, the displacement s as a function of redshift z is given by

$$\frac{ds}{dz} = \frac{c}{H_0} (1+z)^{-1} \left[\Omega_{r,0}(1+z)^4 + \Omega_{m,0}(1+z)^3 + \Omega_{\Lambda,0} \right]^{-\frac{1}{2}} \tag{2}$$

(see e.g. Peacock 1999), where H_0 is the Hubble parameter, $\Omega_{r,\,0}$, $\Omega_{m,\,0}$, and $\Omega_{\Lambda,\,0}$ are the dimensionless energy densities of relativistic matter and radiation, non-relativistic matter, and a cosmological constant (dark energy with an equation of state of $w \equiv -1$), respectively. The subscript '0' denotes that the quantities are measured at present (i.e. $z = 0$). As such, equation (1) becomes

$$\frac{d}{dz} \begin{bmatrix} \mathcal{I} \\ \mathcal{Q} \\ \mathcal{U} \\ \mathcal{V} \end{bmatrix} = (1+z) \left\{ - \begin{bmatrix} \kappa & q & u & v \\ q & \kappa & f & -g \\ u & -f & \kappa & h \\ v & g & -h & \kappa \end{bmatrix} \begin{bmatrix} \mathcal{I} \\ \mathcal{Q} \\ \mathcal{U} \\ \mathcal{V} \end{bmatrix} + \begin{bmatrix} \epsilon_I \\ \epsilon_Q \\ \epsilon_U \\ \epsilon_V \end{bmatrix} \frac{1}{\nu^3} \right\} \frac{ds}{dz} \tag{3}$$

(Chan et al. 2019), where κ, q, u, v are the absorption coefficients, ϵ are the emission coefficients, f is the Faraday rotation coefficient, and g and h are the Faraday conversion coefficients. The invariant Stokes parameters are related to the usual Stokes parameters by $[\mathcal{I}\,\mathcal{Q}\,\mathcal{U}\,\mathcal{V}]^T = [I\,Q\,U\,V]^T/\nu^3$.

In a local frame, the covariant polarized radiative transfer equation in (3) reduces to the standard polarized radiative transfer equation:

$$\frac{d}{ds} \begin{bmatrix} I \\ Q \\ U \\ V \end{bmatrix} = - \begin{bmatrix} \kappa & q & u & v \\ q & \kappa & f & -g \\ u & -f & \kappa & h \\ v & g & -h & \kappa \end{bmatrix} \begin{bmatrix} I \\ Q \\ U \\ V \end{bmatrix} + \begin{bmatrix} \epsilon_I \\ \epsilon_Q \\ \epsilon_U \\ \epsilon_V \end{bmatrix}. \tag{4}$$

The Stokes parameters $[I, Q, U, V]$ are observables, and their combination gives rise to different derived quantities, including the total degree of polarization $\Pi_{tot} = \sqrt{Q^2 + U^2 + V^2}/I \,(\leq 1)$, the degree of linear polarization $\Pi_l = \sqrt{Q^2 + U^2}/I$, the degree of circular polarization $\Pi_c = V/I$, and the polarization angle $\varphi = (1/2)\tan^{-1}(U/Q)$ (see e.g. Rybicki & Lightman 1979).

2.2 Derivation of rotation measure

In the absence of absorption and emission, we can set $\kappa = q = u = v = 0$ and $[\epsilon_I, \epsilon_Q, \epsilon_U, \epsilon_V] = 0$, therefore imposing $dI/ds = 0$, and

$$\frac{d}{ds} \begin{bmatrix} Q \\ U \\ V \end{bmatrix} = - \begin{bmatrix} 0 & f & -g \\ -f & 0 & h \\ g & -h & 0 \end{bmatrix} \begin{bmatrix} Q \\ U \\ V \end{bmatrix}. \tag{5}$$

In situations where the circular polarization is insignificant and the conversion between linear and circular polarization is negligible, we may consider only two linearly polarized Stokes components in

the polarized radiative transfer calculation. The polarized radiative transfer equation then takes a simplified form:

$$\frac{\mathrm{d}}{\mathrm{d}s}\begin{bmatrix} Q \\ U \end{bmatrix} = -\begin{bmatrix} 0 & f \\ -f & 0 \end{bmatrix}\begin{bmatrix} Q \\ U \end{bmatrix}. \tag{6}$$

The Faraday rotation coefficient f is the sole parameter in this equation. It is determined by the properties of free electrons and the magnetic field along the line of sight.

An astrophysical plasma may contain both thermal and non-thermal electrons. If the fraction of non-thermal electrons is small, the conversion between the two linearly polarized Stokes components is determined mainly by the thermal electrons. With only thermal electrons present, the Faraday rotation coefficient is

$$f_{\mathrm{th}} = \frac{\omega_{\mathrm{p}}^2 \cos\theta}{c\,\omega_{\mathrm{B}}} \left(\frac{\omega_{\mathrm{B}}^2}{\omega^2 - \omega_{\mathrm{B}}^2} \right) \tag{7}$$

(Pacholczyk [1977]), where $\omega = 2\pi\nu$ is the angular frequency of radiation, $\omega_{\mathrm{p}} = (4\pi n_{\mathrm{e,th}} e^2/m_{\mathrm{e}})^{1/2}$ is the plasma frequency, $\omega_{\mathrm{B}} = (eB/m_{\mathrm{e}}c)$ is the electron gyro-frequency, $n_{\mathrm{e,\,th}}$ is the thermal electron number density, B is the magnetic field strength, and θ is the angle between the magnetic field vector and the line of sight. Here, c is the speed of light, e is the electron charge, and m_{e} is the electron mass. In the high-frequency limit (i.e. $\omega \gg \omega_{\mathrm{B}}$), the Faraday rotation due to only thermal electrons can be expressed as,

$$f_{\mathrm{th}} = \frac{1}{\pi} \left(\frac{e^3}{m_{\mathrm{e}}^2 c^4} \right) n_{\mathrm{e,th}}\, B_{\parallel}\, \lambda^2, \tag{8}$$

where $B_{\parallel} = |\boldsymbol{B}|\cos\theta$ is the magnetic field along the line of sight and $\lambda = 2\pi c/\omega$ is the wavelength of radiation. The corresponding expression for Faraday rotation due to only non-thermal electrons is

$$f_{\mathrm{nt}} = \frac{1}{\pi} \left(\frac{e^3}{m_{\mathrm{e}}^2 c^4} \right) \zeta(p,\gamma_{\mathrm{i}})\, n_{\mathrm{e,nt}}\, B_{\parallel}\, \lambda^2, \tag{9}$$

where the factor,

$$\zeta(p,\gamma_{\mathrm{i}}) = \frac{(p-1)(p+2)}{(p+1)} \left(\frac{\ln\gamma_{\mathrm{i}}}{\gamma_{\mathrm{i}}^2} \right), \tag{10}$$

for $p > 1$, assuming an isotropic distribution of non-thermal electrons with a power-law energy spectrum of index p (Jones & O'Dell [1977]). The number density of non-thermal electrons is $n_{\mathrm{e,\,nt}}$, and γ_{i} is their low-energy cut-off.

In a plasma consisting of thermal electrons plus non-thermal electrons, the relative strength of their contributions to the Faraday rotation is therefore

$$\frac{f_{\mathrm{nt}}}{f_{\mathrm{th}}} \approx \zeta(p,\gamma_{\mathrm{i}}) \left(\frac{n_{\mathrm{e,nt}}}{n_{\mathrm{e,th}}} \right), \tag{11}$$

provided that neither $n_{\mathrm{e,\,nt}}$ nor $n_{\mathrm{e,\,th}}$ correlates or anticorrelates significantly with $B_{\parallel}$.[2]

From the restrictive polarized radiative transfer equation (6) which only has two linear Stokes components, it can easily be shown that the change in the linear polarization angle along the line

of sight is

$$\frac{\mathrm{d}\varphi}{\mathrm{d}s} = \frac{1}{2}\left(\frac{1}{U^2 + Q^2} \right)\left(Q\frac{\mathrm{d}U}{\mathrm{d}s} - U\frac{\mathrm{d}Q}{\mathrm{d}s} \right) = \frac{f}{2}. \tag{12}$$

With only thermal electrons in a sufficiently weak magnetic field where $\omega_{\mathrm{B}} \ll \omega$, a direct integration of equation (12) with $f = f_{\mathrm{th}}$ yields

$$\varphi(s) = \varphi_0 + \frac{2\pi e^3}{m_{\mathrm{e}}^2(c\,\omega)^2} \int_{s_0}^{s} \mathrm{d}s'\, n_{\mathrm{e,th}}(s')\, B_{\parallel}(s'). \tag{13}$$

Rotation measure (RM) is defined as

$$\mathcal{R} = (\Delta\varphi)\lambda^{-2} = (\varphi - \varphi_0)\,\lambda^{-2}. \tag{14}$$

The polarized radiative transfer equations (4), (5), and (6) are linear, and thus the contributions to the Faraday rotation coefficient by a collection of thermal and non-thermal electrons are additive. The RM for radiation traversing a magnetized plasma between an interval s_0 and s is therefore

$$\mathcal{R}(s) = \frac{e^3}{2\pi m_{\mathrm{e}}^2 c^4} \int_{s_0}^{s} \mathrm{d}s'\, n_{\mathrm{e}}(s')\, \Theta(s')\, B_{\parallel}(s'), \tag{15}$$

where n_{e} is the total electron number density, and $\Theta(s) = 1 - \Upsilon(s)\left[1 - \zeta(p,\gamma_{\mathrm{i}})\right]\big|_s$ is the weighting factor of n_{e} contributing to the Faraday rotation effect, accounting for both thermal and non-thermal electron populations, with $\Upsilon(s)$ the local fraction of non-thermal electrons. If only thermal electrons are present, $\Upsilon(s) = 0$ such that $\Theta(s) = 1$, hence recovering the widely used formula in RM analysis of magnetized astrophysical media (see e.g. Carilli & Taylor [2002]):

$$\mathcal{R}(s) = 0.812 \int_{s_0}^{s} \frac{\mathrm{d}s'}{\mathrm{pc}} \left(\frac{n_{\mathrm{e,th}}(s')}{\mathrm{cm}^{-3}} \right) \left(\frac{B_{\parallel}(s')}{\mu\mathrm{G}} \right)\, \mathrm{rad\,m^{-2}}. \tag{16}$$

3 ROTATION MEASURE FLUCTUATIONS

3.1 Computing rotation measure in a discrete lattice

Practical calculations of polarized radiative transfer in an inhomogeneous medium often require sampling the medium into discrete segments that have small internal variations in physical properties. Suppose we divide the radiation propagation path-length L into N intervals of lengths Δs, i.e. $L = \sum_{i=1}^{N} \Delta s(i)$. Then the integral in equation (15) can be approximated by summing contributions from all segments

$$\mathcal{R}(s) = \frac{e^3}{2\pi m_{\mathrm{e}}^2 c^4} \sum_{i=1}^{N} \Delta s(i)\, n_{\mathrm{e}}(i)\, \Theta(i)\, B_{\parallel}(i), \tag{17}$$

where n_{e}, Θ, and $B_{\parallel}$ are evaluated at the centre of each interval, s_i. If the magnetic fields have uniform strengths and unbiased random orientations, then $B_{\parallel}$ will have a symmetric probability distribution: $P(B_{\parallel}) = P(-B_{\parallel})$. With $\Delta s > 0$, $n_{\mathrm{e}} \geq 0$, and $\Theta \in [0,1]$, the symmetry in the probability distribution of $B_{\parallel}$ implies that the expectation value of RM

$$\langle\mathcal{R}\rangle = \frac{e^3}{2\pi m_{\mathrm{e}}^2 c^4} \sum_{i=1}^{N} \langle \Delta s\, n_{\mathrm{e}}\, \Theta\, B_{\parallel} \rangle\big|_i = 0, \tag{18}$$

where $\langle ... \rangle$ denotes the ensemble average of the variables.

Supposing that n_{e}, Θ, and $B_{\parallel}$ are incoherent among the intervals Δs, then n_{e}, Θ, and $B_{\parallel}$ are the only independent variables for computing the RM of a cell defined by an interval. Moreover, if the medium does not evolve during the radiation's propagation, n_{e},

---

[2]A similar relation was given in Jones & O'Dell ([1977]) for the relative contributions of relativistic and thermal electrons to the Faraday rotation. Their relation is expressed in terms of the spectral index α of the optically thin power-law synchrotron spectrum. The relation (11) here is expressed in terms of the power-law index p of the electron energy distribution, which is intrinsic to the magneto-ionic medium. Note that $\alpha = (p-1)/2$.

Θ, $B_{\parallel}$, and their products are also exchangeable variables. Under the ergodic condition, the ensemble averages of independent and exchangeable variables can be replaced by the averages of over the path-length, i.e. for a sufficiently large N,

$$\langle X \rangle = \frac{1}{N} \sum_{j=1}^{N} X(s_j) = \langle X(s_j) \rangle_s. \tag{19}$$

Thus,

$$\langle \mathcal{R} \rangle = \frac{e^3}{2\pi m_e^2 c^4} N \langle \Delta s \, n_e \, \Theta \, B_{\parallel} \rangle_s = 0. \tag{20}$$

Moreover, if $\boldsymbol{B}$, n_e, and Θ do not correlate with each other, we have

$$\langle \mathcal{R} \rangle = \frac{e^3}{2\pi m_e^2 c^4} N \langle \Delta s \rangle_s \langle n_e \rangle_s \langle \Theta \rangle_s \langle B_{\parallel} \rangle_s = 0. \tag{21}$$

3.2 Rotation measure fluctuations as a restrictive autoregression (AR) process

Note that an observable $\tilde{\mathcal{O}}_k$ on the lattice grid k in an AR(1) (autoregression of order one) process on a 1D lattice is given by the recursive relation:

$$\begin{aligned} \tilde{\mathcal{O}}_k &= \rho \, \tilde{\mathcal{O}}_{k-1} + \varepsilon_k \\ &= \rho \left(\rho \, \tilde{\mathcal{O}}_{k-2} + \varepsilon_{k-1} \right) + \varepsilon_k \\ &\quad \cdots\cdots \\ &= \rho^m \, \tilde{\mathcal{O}}_{k-m} + \sum_{j=0}^{m-1} \rho^j \, \varepsilon_{k-j} \end{aligned} \tag{22}$$

(see e.g. Anderson 1976; Box & Jenkins 1976; Grunwald, Hyndman & Tedesco 1995), where ρ is a parameter, and ε_k is an iid (independent, identically distributed) variable with an expectation value $\mathrm{E}(\varepsilon_k) = \langle \varepsilon_k \rangle = 0$ and a variance $\mathrm{Var}(\varepsilon_k) = [\sigma(\varepsilon_k)]^2$. For a finite or semi-infinite lattice, which is truncated at $j = 0$, at which the observable $\tilde{\mathcal{O}}_0$ is well defined, we can rewrite equation (22) as

$$\tilde{\mathcal{O}}_k = \rho^k \, \tilde{\mathcal{O}}_0 + \sum_{j=1}^{k} \rho^{k-j} \, \varepsilon_j. \tag{23}$$

For a polarized radiation's propagation path consisting of N segments with approximately coherent Faraday rotation properties, the polarization angle at the end of the kth segment is given by

$$\begin{aligned} \varphi_k &= \varphi_{k-1} + \Delta\varphi_k \\ &= \varphi_{k-2} + \Delta\varphi_{k-1} + \Delta\varphi_k \\ &\quad \cdots\cdots \\ &= \varphi_0 + \sum_{j=1}^{k} \Delta\varphi_j, \end{aligned} \tag{24}$$

where $\Delta\varphi_k$ is the rotation of the polarization angle in the kth segment, and the polarization angle measured by the observer is simply φ_N. Comparing equations (24) and (23) reveals that the evolution of the polarization angle along the radiation's propagation is an AR(1) process with a constant parameter $\rho = 1$, provided that $\langle \Delta\varphi_j \rangle = 0$ and that $\mathrm{Var}(\Delta\varphi_j)$ is well defined and computable. An AR(1) process is a Markov process (see Anderson 1976), and an AR(1) process with $\rho = 1$ is also known as a simple random walk.

The rotation measure across the propagation path of the radiation is $\mathcal{R}|_N = (\varphi_N - \varphi_0)\lambda^{-2}$. Hence, from equation (20), we obtain

$$\left\langle \sum_{j=1}^{N} \Delta\varphi_j \right\rangle_s = \lambda^2 \, \langle \mathcal{R} \rangle_s = 0. \tag{25}$$

As the expectation value and the variance of $(\varphi_N - \varphi_0)$ are

$$\mathrm{E}\left[\varphi_N - \varphi_0 \right] = 0; \tag{26}$$

$$\mathrm{Var}\left[\varphi_N - \varphi_0 \right] = N \, \sigma^2, \tag{27}$$

respectively, with $\sigma^2 = \langle \Delta\varphi_j^2 \rangle$, the standard deviation of $\mathcal{R}$ in the radiation's propagation direction is therefore

$$\begin{aligned} \sigma_{\mathcal{R}} &= \sqrt{N} \, \left[\langle \Delta\varphi_j^2 \rangle \right]^{1/2} \lambda^{-2} \\ &= \frac{e^3 \sqrt{N}}{2\pi m_e^2 c^4} \, \left[\langle \Delta s^2 \, n_e^2 \, \Theta^2 \, B_{\parallel}^2 \rangle \right]^{1/2} \\ &= \frac{e^3 \sqrt{N}}{2\pi m_e^2 c^4} \, \left[\langle \Delta s^2 \, n_e^2 \, \Theta^2 \, B_{\parallel}^2 \rangle_s \right]^{1/2}. \end{aligned} \tag{28}$$

Note that the RMF along a radiation propagation path consisting of coherent segments is proportional to the square root of the number of the segments ($\sqrt{N} = \sqrt{L/\langle \Delta s \rangle_s}$), a characteristic of a simple random-walk process, where the root-mean-square displacement is proportional to the square root of the number of steps. Here, the root mean square of properties within a step size is $\left[\langle \Delta s^2 \, n_e^2 \, \Theta^2 \, B_{\parallel}^2 \rangle_s \right]^{1/2}$. In the specific condition that the interval segments have equal length, $\overline{\Delta s}$, and $(n_e \, \Theta)$ does not vary along the line of sight, equation (28) becomes

$$\sigma_{\mathcal{R}} = \frac{e^3}{2\pi m_e^2 c^4} \sqrt{\frac{L}{\overline{\Delta s}}} \, \overline{\Delta s} \, n_e \, \Theta \, \left[\langle B_{\parallel}^2 \rangle_s \right]^{1/2}. \tag{29}$$

A similar but more rigorous expression can be obtained if there is no correlation between electron number density and the magnetic fields. In this case, equation (28) becomes

$$\sigma_{\mathcal{R}} = \frac{e^3}{2\pi m_e^2 c^4} \sqrt{\frac{L}{\overline{\Delta s}}} \, \overline{\Delta s} \, \overline{n_e \, \Theta} \, \left[\langle B_{\parallel}^2 \rangle_s \right]^{1/2}, \tag{30}$$

with $\overline{n_e \, \Theta}$ denoting the mean value of $(n_e \, \Theta)$. Additionally, in the presence of only thermal electrons, then $\Theta = 1$ uniformly, and

$$\begin{aligned} \sigma_{\mathcal{R}} &= \frac{e^3}{2\pi m_e^2 c^4} \sqrt{\frac{L}{\overline{\Delta s}}} \, \overline{\Delta s} \, \overline{n}_{e,\mathrm{th}} \, B_{\parallel \mathrm{rms}} \\ &= 0.812 \sqrt{\frac{L}{\overline{\Delta s}}} \left(\frac{\overline{\Delta s}}{\mathrm{pc}} \right) \left(\frac{\overline{n}_{e,\mathrm{th}}}{\mathrm{cm}^{-3}} \right) \left(\frac{B_{\parallel \mathrm{rms}}}{\mu\mathrm{G}} \right) \, \mathrm{rad \, m}^{-2}. \end{aligned} \tag{31}$$

Most observational or numerical studies use either one of the expressions given in equations (30), and (31) in their RM fluctuation analysis. These include investigations of magnetic fields in galaxy clusters or in large-scale structures (e.g. Sokoloff et al. 1998; Blasi, Burles & Olinto 1999; Dolag et al. 2001; Govoni & Feretti 2004; Subramanian, Shukurov & Haugen 2006; Cho & Ryu 2009; Sur 2019). Note that the two expressions above are not always explicitly distinguished in studies of RM fluctuations. The $\sigma_{\mathcal{R}}$ derivations from equation (28) to equations (29), (30), and (31) rely on subtly different assumptions regarding the electron density spatial distributions and their relation or correlation with the magnetic fields. For instance, it matters whether local quantities are multiplied before spatial averaging, or averaged separately then multiplied. Note also that, in reality, the condition of constant electron number density, or/and the condition of electron number density and magnetic field being uncorrelated, are generally not satisfied. We should therefore bear in mind which underlying assumptions have been used, and they should be stated explicitly when interpreting the magnetic field structures using the observed RM statistics. Furthermore, while $\sigma_{\mathcal{R}}$
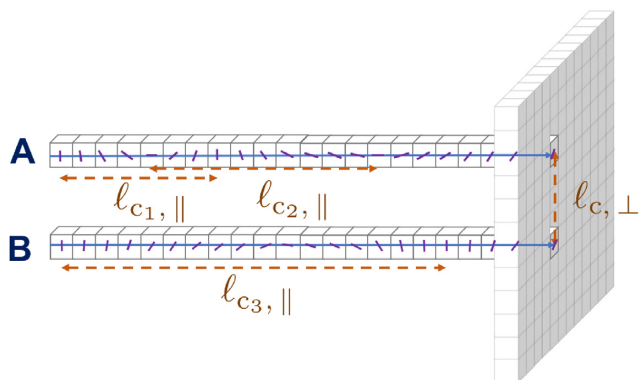
Figure 1. Illustration of a case where $\sigma_{x,\perp} \neq \sigma_{x,\|}$, emphasizing that polarizations are modified along the line of sight, but what we observe is only the resulting angle on the orthogonal image plane. In this demonstration, line of sight **A** exhibits two characteristic lengths of polarization fluctuation, $\ell_{c_1,\|}$ and $\ell_{c_2,\|}$, as illustrated by the number of cells spanning a full rotation, while for line of sight **B**, $\ell_{c_3,\|}$. None of these coincides with $\ell_{c,\perp}$ on the image plane.

is observed on the sky plane, it is calculated over the radiation's propagation path, with the application of a random-walk model along the line of sight and invoking other explicit assumptions we made above.

3.3 Fluctuations of density and magnetic fields in parallel and in perpendicular directions

The polarization of radiation at a location on the sky plane, and hence the celestial sphere, is determined by the magneto-ionic properties of plasma along the line of sight (specified by the propagation unit vector $\hat{\boldsymbol{k}}$). On cosmological scales, the transfer of radiation along the line of sight is the transfer of radiation from the past to the present. Consequently, the statistical properties of the observed polarization signatures across a sky plane depend on two factors: (i) the spatial variations of the magneto-ionic plasma properties at different cosmological epochs, and (ii) the temporal variations of the magneto-ionic plasma properties as the Universe evolved. Note that these two factors are not always mutually independent. It is their convolution that will determine the variations of the observable variables along the ray as it propagates (i.e. in $\hat{\boldsymbol{k}}$ direction, denoted by $_\|$) and the variations of the observable variables among the collection of rays reaching the sky plane (i.e. in directions $\perp$ to $\hat{\boldsymbol{k}}$). More importantly, there is no guarantee that these two types of fluctuations are statistically identical. In other words, if we use a simple representation with two independent orthogonal components, designated to be parallel and perpendicular to $\hat{\boldsymbol{k}}$, we cannot simply assume that $\sigma_{x,\perp} = \sigma_{x,\|}$, where the quantity $x \in \{Q, U, V, \Delta\varphi, \text{ or } \mathcal{R}\}$. In general, we have two separate correlation lengths, $\ell_\|$ and $\ell_\perp$, for each plasma quantity, e.g. the electron number density n_e (which is a scalar) and the magnetic field $\boldsymbol{B}$ (which is a vector). See Fig. 1 for an illustration.

The question now is whether we can take a correlation length derived from a polarization signature across the sky plane as the characteristic correlation length-scale over which the cosmological magnetic fields vary spatially or, alternatively, over time. First, the polarized radiative transfer equation shows that the rotation of the polarization angle only depends on the magnetic field parallel to the line of sight, i.e. $\boldsymbol{B}_\|$. The perpendicular component of the magnetic field $\boldsymbol{B}_\perp$ is irrelevant in this respect. Therefore, in each individual
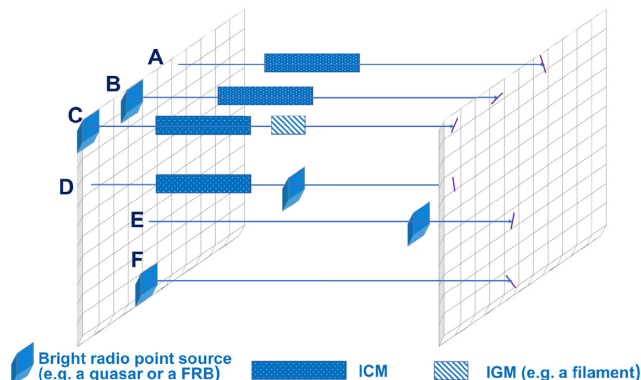
Figure 2. Illustration of how different astrophysical conditions give rise to different polarization fluctuations due to e.g. (i) the presence or absence of bright background sources (lines of sight **A** and **B**), (ii) the presence or absence of multiple sources with different Faraday depths (lines of sight **B** and **C**), (iii) different positional orders of sources (lines of sight **B** and **D**), and (iv) change of radiation frequency due to the Universe's expansion, and/or the presence of sources either at low or high redshift (lines of sight **E** and **F**).

ray, the local polarization fluctuations are only caused by the fluctuations of the parallel field component, $\boldsymbol{B}_\|$, and the fluctuations of the electron number density n_e and energy distribution.

Secondly, the fluctuations of polarization properties along individual rays are not directly observable. Instead, observations reveal a 'polarization map' on the celestial sphere, which represents the polarization signatures of a collection of end-points of the path-integrated polarized rays. If the rays are independent, we would observe variations in the polarization signatures, such as the RM fluctuations, even when the magneto-plasma is statistically spatially uniform at any cosmological epoch. In this situation, the observed RM fluctuations reflect the convolution of the fluctuations in $|\boldsymbol{B}_\||$ and n_e along the line of sight, i.e. not simply an effect arising from the presence of spatial structures. Note that there are additional subtleties in assessing the local variations of polarization signature along a ray. Suppose that the electron number density and its energy spectrum are uniform in both space and time, there still exists an ambiguity in determining the fluctuation of the magnetic field $\boldsymbol{B}$, as the polarization angle rotates depending on value of $|\boldsymbol{B}_\||$, which equals to $|\boldsymbol{B}|\cos\theta$, at an unknown angle $\theta = \cos^{-1}(\hat{\boldsymbol{k}} \cdot \hat{\boldsymbol{B}})$. Thus, there are two aspects in the magnetic field fluctuations: one concerning the field magnitudes, and another concerning the field orientations. Magnitude fluctuations and orientation fluctuations can arise from different processes. For instance, the variations in the magnetic field orientation $\hat{\boldsymbol{B}}$ may indicate the characteristic size of the astrophysical system or the magnetic sub-domain of the cosmic magneto-ionic plasma, while the variations in the magnetic field magnitude $|\boldsymbol{B}|$ along the line of sight would inform us about the changes in the global magnetic energy density as the Universe evolves. Fluctuations of $\hat{\boldsymbol{B}}$ and those of $|\boldsymbol{B}|$ can arise from different mechanisms and/or operate on different characteristic time-scales. Thus, $\sigma_{|\boldsymbol{B}|}\big|_{\|, \text{ or } \perp} = \sigma_{\hat{\boldsymbol{B}}}\big|_{\|, \text{ or } \perp}$ do not usually hold.

Fig. 2 illustrates some example scenarios that give rise to different observational polarization signals .[3] The types and number

---

[3]Inferring the magneto-ionic properties of the line-of-sight sources and the intervening plasmas from the polarized sky data, which has a $(2+1)$D structure, where the '+1' corresponds to the time axis or cosmological redshift, is an inverse problem. In forward theoretical modelling, the

of sources, and the magneto-ionic properties of the intervening plasmas vary along each line of sight and vary among the lines of sight across the sky. Magnetic fields are vectors, and therefore possess two structural traits: one in the field strength (or energy density), and another in the field orientation. Both aspects are essential to determine the properties of all-sky polarization. Faraday rotation also depends on the line-of-sight electron number densities, and the electron number densities and the magnetic fields are usually interdependent. Depending on what mechanisms generate and/or amplify the magnetic fields, local and non-local correlations between the two quantities could occur. As such, we cannot simply take the face values of the correlation lengths obtained from RM fluctuation analyses as they appear, without careful consideration. In the analysis of cosmological-scale magnetism we also need to consider effects due to cosmological expansion. Large-scale magnetic fields would evolve with the cosmological structure (see e.g. Dolag, Vogt & Enßlin 2005; Cho & Ryu 2009; Barnes, Kawata & Wu 2012; Ryu et al. 2012; Marinacci et al. 2015; Barnes et al. 2018; Katz et al. 2019). Covariant PRT calculations (Chan et al. 2019) are therefore essential, if we wish to take full account of all the magneto-ionic plasma effects throughout the evolutionary history of the Universe, providing insights and theoretical bases for proper interpretation of the statistical RM analyses of the observed polarized sky.

4 RESULTS AND DISCUSSION: VARIANCE OF RM FLUCTUATIONS

4.1 Assessing the rotation measure fluctuation approach

The formula in equation (31) is commonly used in RM fluctuation analysis for probing the structures in large-scale magnetic fields. Here we assess when the formula is justified and when it deserves caution. The formula contains two variables related to n_e and $\boldsymbol{B}$, and our assessment will focus on their spatial distribution properties. We perform Monte Carlo simulations to compute the RM fluctuations. We consider simulated cubes of Mpc size with mock thermal electron number density (d) and magnetic field strength (b) with uniform (U), Gaussian (G), fractal (F), and lognormal (L) distributions. Each simulation is specified by a four-letter label. For instance, 'UdGb' stands for uniformly distributed densities and Gaussian-distributed magnetic field strengths with random orientations. The Mersenne Twister (MT, Matsumoto & Nishimura 1998) is implemented to generate uniformly distributed pseudo-random numbers, $Z \in (0, 1]$, which transform into the G-, F-, and L-distributed variates according to the specification.

The cubes are discretized into 256^3 voxels, each having an equal linear length $\overline{\Delta s}$ on the three sides. The magnetic field and the thermal electrons are specified according to the assigned distributions. Their values are normalized such that they are of a similar order to those observed in galaxy clusters: $\langle n_{e,th} \rangle = 10^{-3} \, \text{cm}^{-3}$, $B_{rms} = 1 \, \mu\text{G}$, and $L = 1 \, \text{Mpc}$ (e.g. Cho & Ryu 2009). The total thermal electron number density and the total magnetic energy in the whole simulation box, regardless of the magneto-ionic distribution, are $256^3 \times 10^{-3} = 16777.216 \, \text{cm}^{-3}$ and $|\boldsymbol{B}|^2 = 256^3 = 16777216 \, (\mu\text{G})^2$, respectively. This ensures uniformity between

polarization signals are, however, determined by the cosmological polarized radiative transfer, which is in a $(3 + 1)$D format, where the line-of-sight direction also aligns with the axis of cosmological time.

the model cubes, which enables direct comparisons between the simulations.

To compute the RM, we sum the contributions along the lines of sight, $\boldsymbol{x}$, $\boldsymbol{y}$, and $\boldsymbol{z}$, using the discretized expression of equation (16) in terms of lattice units (i, j, k),

$$\mathcal{R}_\perp = 0.812 \sum_\parallel \frac{\overline{\Delta s}}{\text{pc}} \left[\left(\frac{n_{e,th}(i, j, k)}{\text{cm}^{-3}} \right) \left(\frac{B(i, j, k)}{\mu\text{G}} \right) \right]_\parallel \text{rad m}^{-2} .$$

(32)

The standard deviation $\varsigma_{\mathcal{R}_\perp}$ across the simulated sky plane is then computed and compared to the longitudinal standard deviation given in equation (31).

4.1.1 Modelling magnetic fields

We consider magnetic fields with random orientations and no spatial correlation. They are therefore unit vectors: $\hat{B}_x = \sin\theta\cos\phi$, $\hat{B}_y = \sin\theta\sin\phi$, and $\hat{B}_z = \cos\theta$, with $\cos\theta \in (-1, 1]$ and $\phi \in (0, 2\pi]$ in a uniform distribution. The field strength on the other hand has a uniform, non-solenoidal (Ub*) or a uniform, solenoidal (Ub), or a Gaussian (Gb) distribution. The normalization is such that the r.m.s. value $B_{rms} = 1 \, \mu\text{G}$. Hence, we have $B_{\parallel rms} = B_{rms}/\sqrt{3} \simeq 0.577 \, \mu\text{G}$. The Gaussian distribution is generated using the Box–Muller transform in the usual Monte Carlo simulations. The simulated magnetic fields are then cleaned in Fourier space with the application of a divergence-free ($\nabla \cdot \boldsymbol{B} = 0$) filter: $B_i(k_m) = (\delta_{ij} - k_i k_j / k^2) \tilde{B}_j(k_m)$ (Balsara 1998). As the process removes the field component parallel to $\boldsymbol{k}$, the total magnetic energy stored in the cube shrinks to 2/3 of its original value. To compensate for the energy loss by the filtering process, the field components are rescaled by a factor of $\sqrt{3/2}$. An inverse Fourier transform is then conducted to obtain the divergence-free ('solenoidal') magnetic field in the configuration space (see Appendix A).

We also note that the divergence-free filtering process introduces a residual dipole, which has a preferred orientation, depending on how the filtering process is executed. To suppress this dipole structure, we employ a quick-fix solution[4] using a superposition of three independent, orthogonal field realizations. We then renormalize the resultant field from the superposition by a $\sqrt{1/3}$ scaling factor. Since the realizations prepared as such are divergence free in real (configuration) and Fourier space, their linear superpositions in real and Fourier space[5] will also be divergence free.

---

[4] In a more proper treatment, we would need a superposition of three antiparallel pairs of independent, orthogonal field realizations in order to completely remove the dipole. The process would then leave a residual quadrupole. None the less the quick-fix solution that we employ to suppress the dipole is sufficient for the purpose of this demonstrative study. In reality, the divergence filtering is not always necessary before radiative transfer, as the magnetic fields output by a detailed magnetohydrodynamic simulation (see e.g. Marinacci et al. 2015, 2018; Barnes et al. 2018) should be divergence free, at least in principle.

[5] Note that in the execution of Fourier transform process, we do not consider an infinite span of the configuration space. The restriction of the electron number density and magnetic field structure within a finite volume is equivalent to the introduction of a cubic window function to an infinite configuration space. Thus, the density distribution and the magnetic field structure that we obtain in the Fourier representation are the convolutions of the cubic window function with the electron number density distribution and the magnetic field structure.

4.1.2 Modelling free-electron number density

We consider four model electron number density distributions: uniform (Ud), Gaussian (Gd), lognormal (Ld), and fractal (Fd). For the uniform distribution, the electron number density is set to be one unit in each cell. For the Gaussian distribution, we apply a Box–Muller transform, setting the standard deviation to 0.2 times the mean 10^{-3} cm^{-3}, so that there are only a few negative numbers, which can be converted to positives by simply taking the absolute. The lognormal distribution is generated by taking the exponential function of Gaussian-distributed random numbers. For a fractal model, we generate random phases (k_x, k_y, k_z) in Fourier space. We then apply a power-law filter $|\boldsymbol{k}|^{-5/3}$ to mimic a Kolmogorov-like turbulence spectrum (1941a, b). Simulations predict various kinds of turbulence in clusters and cosmic filaments (e.g. Iapichino et al. 2011). Scaling laws originally derived for incompressible media also turn out to be a good approximation for compressible turbulence in subsonic regions of real observed or numerically simulated IGM (see e.g. Schuecker et al. 2004; Miniati 2014; Nakwacki et al. 2016; White et al. 2019).[6] In our model, we apply frequency cut-offs as in Saxton et al. (2005): we impose $k_{max} = N/2$ to prevent excessively sharp contrasts at voxel scale, and $k_{min} = 8$ to prevent any single density peak dominating. The inverse fast Fourier transform yields a fractal-like spatial structure with normally distributed local values $\mathcal{N}$. Dimensionless positive densities are obtained by taking $\exp(\alpha\mathcal{N}/\mathcal{N}_{max})$, where the contrast factor $\alpha = 4$ and $\mathcal{N}_{max}$ is a fiducial maximum fluctuation (Elmegreen, Seiden & Elmegreen 1989; Elmegreen 2002). Lastly we obtain the various astrophysical configurations of thermal electron number densities by normalizing $\langle n_{e, th} \rangle$ of each box to 10^{-3} cm^{-3}.

4.1.3 RM dependence on the density and magnetic field structures

We calculate synthetic RM maps by integrating along lines of sight $\boldsymbol{x}$, $\boldsymbol{y}$, and $\boldsymbol{z}$ using equation (32) through various distributions of thermal electron number densities and magnetic field strengths. The RM maps from the GdGb and UdUb* distributions are indistinguishable from a simple eyeball test (see Fig. 3), even though the maps are generated from distinct distributions of number densities and magnetic field strengths. GdGb is commonly assumed in astrophysical scenarios, whereas UdUb* is simply unrealistic because the magnetic fields are non-solenoidal. The resulting RM maps are similar across all lines of sight, implying that it is non-trivial to characterize the thermal number densities and the magnetic field strengths from the observed RM fluctuations alone.

We compare models quantitatively in Table 1. We calculate the line-of-sight longitudinal dispersions using equation (31) and obtain $\sigma_{\mathcal{R}}^{xy} \simeq \sigma_{\mathcal{R}}^{xz} \simeq \sigma_{\mathcal{R}}^{yz} \simeq 29.3$ rad m^{-2} in all cases, indicating that this type of RM fluctuation formula cannot distinguish between the different distributions of number densities and magnetic field strengths. The tiny variations in the least significant figures of $\sigma_{\mathcal{R}}^{xy}$, $\sigma_{\mathcal{R}}^{xz}$, and $\sigma_{\mathcal{R}}^{yz}$ are due to the numerical noise and random differences in the generated realizations. Table 1 also shows that line-of-sight and sky transverse fluctuations match reasonably well ($\sigma_{\mathcal{R}} \simeq \varsigma_{\mathcal{R}}$) in the cases of UdUb*, UdUb, and UdGb, indicating that the widely used RM fluctuation formula is applicable for uniformly distributed densities and magnetic field strengths with uniform distributions and Gaussian distributions. However, for GdUb, GdGb, FdUb,

FdGb, LdUb, and LdGb $\sigma_{\mathcal{R}} < \varsigma_{\mathcal{R}}$, meaning that the RM fluctuation formula is inadequate in situations with Gaussian, fractal, or lognormal density distributions. The disagreement between $\sigma_{\mathcal{R}}$ and $\varsigma_{\mathcal{R}}$ is at the level of ~ 2 per cent, ~ 25 per cent, and ~ 40 per cent, respectively, for G, F, and L density models. For a comparison, we note that Bhat & Subramanian (2013) calculated the evolving RM properties of the ICM in fluctuation dynamo simulations, and found that $\varsigma_{\mathcal{R}}$ was ~ 10 per cent–15 per cent above some statistical indicators of RMF ($\approx \sigma_{\mathcal{R}}$). In their models, the evolving magnetic features seemed to be more influential than the density variations.

Notably, both our RMS model and explicit RT simulation cannot distinguish the difference between solenoidal and non-solenoidal fields, as shown by $\sigma_{\mathcal{R}}(\text{UdUb*}) \simeq \sigma_{\mathcal{R}}(\text{UdUb}) \simeq 29.3$ rad m^{-2}. Our calculations also show that the sky planar fluctuations: $\varsigma_{\mathcal{R}}(\text{UdUb*}) \simeq \varsigma_{\mathcal{R}}(\text{UdUb}) \simeq \varsigma_{\mathcal{R}}(\text{UdGb})$, $\varsigma_{\mathcal{R}}(\text{GdUb}) \simeq \varsigma_{\mathcal{R}}(\text{GdGb})$, $\varsigma_{\mathcal{R}}(\text{FdUb}) \simeq \varsigma_{\mathcal{R}}(\text{FdGb})$, and $\varsigma_{\mathcal{R}}(\text{LdUb}) \simeq \varsigma_{\mathcal{R}}(\text{LdGb})$. The Fourier transform and inverse Fourier transform are part of the divergence cleaning process. Note that the Fourier transform of uniformly distributed fields in a finite volume gives a 3D sinc function (in the Cartesian coordinate).

For a more detailed characterization of the RM distributions, we calculate the histograms and cumulative distribution functions (CDFs) of the RM maps from every line of sight through the UdUb*, UdUb, UdGb, GdUb, GdGb, FdUb, FdGb, LdUb, and LdGb distributions. For each cube, the histograms and CDFs along lines of sight $\boldsymbol{x}$, $\boldsymbol{y}$, and $\boldsymbol{z}$ coincide, confirming that isotropy is preserved in each box (also demonstrated by the results in Table 1, where $\sigma_{\mathcal{R}}^{xy} \simeq \sigma_{\mathcal{R}}^{xz} \simeq \sigma_{\mathcal{R}}^{yz}$ for all simulations). We set GdGb(z) as the basis CDF and calculate its numerical difference from the CDFs of the rest of the models. The CDFs at every line of sight are almost indistinguishable in each case of GdGb, UdUb*, UdUb, UdGb, and GdUb, as shown by the tiny fluctuations in the zero line (Fig. 4). The CDFs of FdUb, FdGb, LdUb, and LdGb deviate significantly from the basis CDF.

Using the numerical CDF curves, we perform a Kolmogorov–Smirnov (KS) test with the null hypothesis being that the two RM samples, observed either in the $\boldsymbol{x}$, $\boldsymbol{y}$, or $\boldsymbol{z}$ direction, are drawn from the same distribution. The KS test is non-parametric and reports the maximum value of absolute (vertical) difference between two CDFs (see e.g. Press et al. 2007). We calculate the KS statistics which are summarized in Table 2. We obtain $D \ll 1$ and p-value probabilities in the range of 0.2–0.6, favouring the null hypothesis since $p > 0.05$. Our KS tests do not show evidence of anisotropy.

In addition, we consider a fractal medium with two density phases (hereafter referred to as cloudy models), mimicking the typical environments in the ICM/ISM (see Appendix B). We consider various cloud volume-filling factors $f = 10^{-2}, 10^{-3}, 10^{-4}, 10^{-5}$, and 10^{-6}, corresponding to Cd2, Cd3, Cd4, Cd5, and Cd6, respectively. Figs 5 and 6 show the $\log_{10}$ cross-sections and column densities of Cd3 and Cd5, respectively. The cross-sections are a slice taken from the cloudy models Cd3 and Cd5 at $x = 128$, $y = 128$, and $z = 128$. The cross-sections and column densities show the non-uniformity of the diffuse media and the cloud phases. The cloudy models are fairly isotropic along every line of sight, with Cd3 being more dense than Cd5, as indicated by the larger number of bright specks embedded within the cloudy media. Fig. 7 shows that the RM maps of the Cd2Gb and Cd2Ub* distributions are indistinguishable, despite the distinction between the distributions of magnetic field strengths, especially with Ub* being non-solenoidal and unphysical. Moreover, our calculations in Table 3 show that the RMS statistics are unable to tell the cloudy features apart, in spite of Cd2–6 having

---

[6]The alternative extreme, of shock-compressed supersonic turbulence, yields steeper spectra $\sim k^{-2.1}$ (e.g. Lee, Lele & Moin 1991; Federrath 2013).
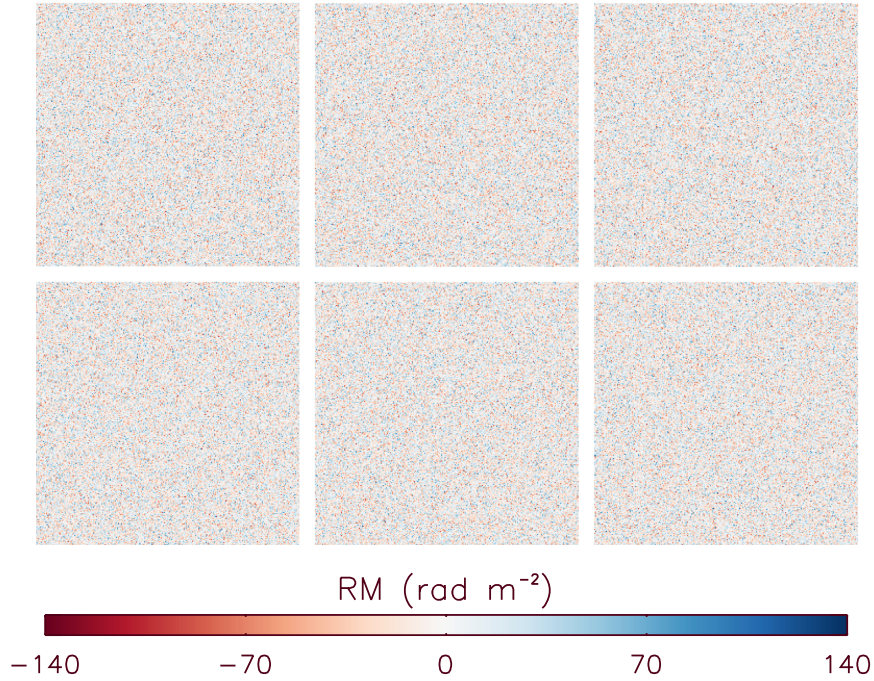
Figure 3. Synthetic RM maps of one realization of GdGb (top) and UdUb* (bottom) in the xy (left), xz (middle), and yz (right) planes.

Table 1. The dispersion of RM, $\sigma_{\mathcal{R}}^{xy}$, $\sigma_{\mathcal{R}}^{xz}$, and $\sigma_{\mathcal{R}}^{yz}$, calculated along lines of sight z, y, and x, respectively, as light travels through various configurations of magnetized, thermal plasma. The transverse dispersion is calculated from the RM maps over the sky plane: $\varsigma_{\mathcal{R}}^{xy}$, $\varsigma_{\mathcal{R}}^{xz}$, and $\varsigma_{\mathcal{R}}^{yz}$. The last three columns show the ratios of the longitudinal dispersion to the transverse dispersion. The realizations are normalized to the order of magnitude typically found in galaxy clusters: $\langle n_{e,th}\rangle \sim 10^{-3}$ cm^{-3}, $B_{rms} \sim 1$ μG, and $L \sim 1$ Mpc. The magnetic fields are strictly divergence free, except for Ub*.

Distribution		Longitudinal (equation 31)			Sky transverse (equation 32)			Ratio		
		$\sigma_{\mathcal{R}}^{xy}$	$\sigma_{\mathcal{R}}^{xz}$	$\sigma_{\mathcal{R}}^{yz}$	$\varsigma_{\mathcal{R}}^{xy}$	$\varsigma_{\mathcal{R}}^{xz}$	$\varsigma_{\mathcal{R}}^{yz}$	$\sigma^{xy}/\varsigma^{xy}$	$\sigma^{xz}/\varsigma^{xz}$	$\sigma^{yz}/\varsigma^{yz}$
Ud	Ub*	29.2971	29.2975	29.2962	29.2861	29.3151	29.3042	1.0004	0.9994	0.9997
Ud	Ub	29.2962	29.2977	29.2970	29.3101	29.3198	29.3278	0.9995	0.9993	0.9990
Ud	Gb	29.2965	29.2965	29.2979	29.3231	29.2934	29.3299	0.9991	1.0001	0.9989
Gd	Ub	29.2982	29.2961	29.2966	29.9263	29.8972	29.8994	0.9790	0.9799	0.9798
Gd	Gb	29.2970	29.2973	29.2966	29.9113	29.8854	29.8902	0.9795	0.9803	0.9801
Fd	Ub	29.2987	29.2965	29.2956	39.1187	39.1392	39.1134	0.7490	0.7485	0.7490
Fd	Gb	29.2975	29.2966	29.2968	39.1185	39.1357	39.1186	0.7489	0.7486	0.7489
Ld	Ub	29.2969	29.2968	29.2972	48.3524	48.3218	48.3327	0.6059	0.6063	0.6062
Ld	Gb	29.2975	29.2964	29.2970	48.3058	48.3017	48.3146	0.6065	0.6065	0.6064

different volume-filling factors. In particular, the RMS statistics for various distributions of Cd and b are $\sigma_{\mathcal{R}} \simeq 29.3$ rad m^{-2}, which is similar to the RMS statistics for various distributions of our single-phase models in Table 1, indicating that the RMS method cannot distinguish between a range of different clumpy (or smooth) configurations of density and magnetic fields. We also calculate the sky-transverse standard deviations and find that, with the exception of the overcast model Cd2, the $\varsigma_{\mathcal{R}}$ decreases with decreasing volume-filling factor. This is expected since the scatter should be less with fewer clouds (and we approach the L lognormal models as $f \rightarrow 0$). Clumpiness always causes $\varsigma_{\mathcal{R}} > \sigma_{\mathcal{R}}$, and often by large multiples (with relative differences up to 94 per cent). Furthermore, comparing the dispersions between the longitudinal direction and the sky transverse direction, the cloudy models in Table 3 show a greater scatter than the Ud, Gd, Fd, and Ld models did in Table 1. The variability of standard deviations may be attributed to the random shapes and orientations of the clouds.

We also calculate histograms (not shown) to characterize the RM distributions from every line of sight through the Cd2Ub*, Cd2Ub, Cd2Gb, Cd3Ub*, Cd3Ub, Cd3Gb, Cd4Ub*, Cd4Ub, Cd4Gb, Cd5Ub*, Cd5Ub, Cd5Gb, Cd6Ub*, Cd6Ub, and Cd6Gb distributions. For each cube, the histograms along lines of sight x, y, and z coincide, confirming that isotropy is preserved in each box, which is also shown by $\varsigma_{\mathcal{R}}^{xy} \simeq \varsigma_{\mathcal{R}}^{xz} \simeq \varsigma_{\mathcal{R}}^{yz}$ in Table 3.

The results from the KS tests are summarized in Table 4. The KS statistics do not show evidence of anisotropy. Using GdGb(z) as the basis CDF, we calculate its numerical difference from the CDFs of the cloudy, magnetized models in Fig. 8. These panels are almost indistinguishable between different configurations of magnetic fields, e.g. the numerical difference trends for Cd3Ub*(x, y, z), Cd3Ub(x, y, z), and Cd3Gb(x, y, z) look similar to each other. This suggests that the RMs are more dependent on the cloudy structures, rather than the magnetic field configurations since the
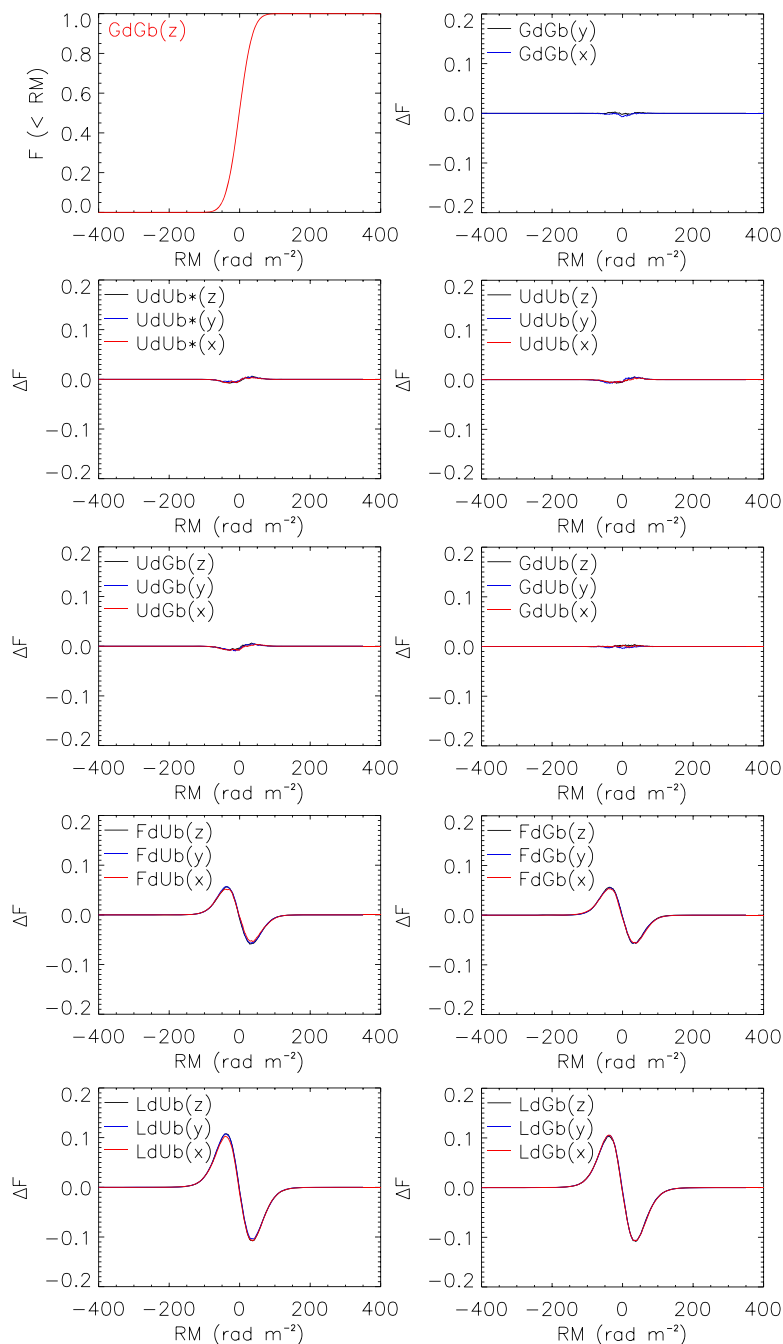
Figure 4. Top-left panel showing the CDF of GdGb(z) as a reference to calculate the numerical differences with the CDFs of GdGb(y), GdGb(x) as well as UdUb*, UdUb, UdGb, GdUb, FdUb, FdGb, LdUb, and LdGb for every line of sight. The CDFs are almost identical in all cases, except for models with fractal and lognormal density distributions.

density variations are of orders of magnitude within each cube, while the dynamic variation of the magnetic field is relatively smaller. Notably the CDFs of Cd2 show the largest deviation from the basis CDF, whereas the CDFs for the rest of the models, apart from Cd3, are almost indistinguishable. This may be a consequence of a scarcity of clouds in Cd4, 5, and 6.

Hence, from our results above, the widely used RM fluctuation formula (RMS statistics) is valid when all of the following conditions hold: (i) a random field produces random Faraday rotation, (ii) there exists a meaningful characteristic thermal electron number density, (iii) there exists a uniform or Gaussian distribution of magnetic field strengths, (iv) the field is isotropic, and (v) the density and the magnetic field are not correlated. In situations where some of these criteria are not met, the RMS statistics would be inadequate to be used to interpret the magnetic field properties from the RM analyses. Discrepancies could in principle be large in some environments such as cluster cores where multiphase features are obvious in other wavebands (e.g. Conselice, Gallagher & Wyse 2001) or faint cluster outskirts where clumpiness is conjectured (e.g. Urban et al. 2014).

Table 2. The KS statistics D and p-value probabilities corresponding to various configurations in Table 1.

Distribution		D			p-value		
		xy and xz	xy and yz	xz and yz	xy and xz	xy and yz	xz and yz
Ud	Ub*	0.0044	0.0048	0.0045	0.5707	0.4763	0.5460
Ud	Ub	0.0052	0.0047	0.0052	0.4272	0.5502	0.4364
Ud	Gb	0.0052	0.0055	0.0057	0.4255	0.3654	0.3712
Gd	Ub	0.0052	0.0048	0.0052	0.4240	0.5123	0.4509
Gd	Gb	0.0050	0.0051	0.0051	0.4696	0.4359	0.4275
Fd	Ub	0.0047	0.0072	0.0072	0.5110	0.1549	0.1421
Fd	Gb	0.0049	0.0068	0.0071	0.5052	0.1696	0.1658
Ld	Ub	0.0050	0.0050	0.0050	0.4833	0.4662	0.4644
Ld	Gb	0.0049	0.0045	0.0049	0.4806	0.5550	0.4865
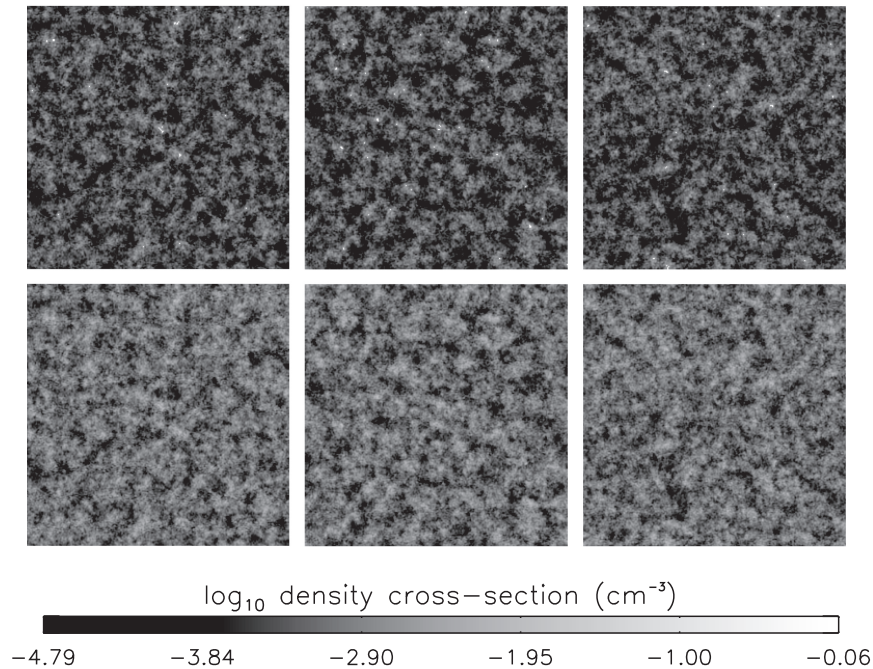
Figure 5. Cross-sections of Cd3 (top) and Cd5 (bottom) at $x = 128$ (left), $y = 128$ (middle), and $z = 128$ (right).

## 4.2 Interpreting magnetic field properties from polarization analyses

4.2.1 Ambiguity in the polarization angle

The inference of RM from observations of linear polarization is subjected to an $n\pi$ ambiguity in its direction (Ruzmaikin & Sokoloff 1979). For a clean line of sight with a single point source, the polarization angle φ and the wavelengths λ satisfy a relationship: $\varphi = \varphi_0 + \mathcal{R}\lambda^2$, fitting the observation for the intrinsic polarization angle φ_0 and the slope $\mathcal{R}$ gives the rotation measure. The foreground magnetic field structure can be inferred from the RM if the emission measure is known. In practice, the measured polarization angle φ can only be constrained between 0 and π, hence there is an ambiguity of $\pm n\pi$, where n is an integer, thus causing a problem in determining φ_0 and $\mathcal{R}$.

Early efforts were taken to resolve this ambiguity by imposing a search limit for the best RM from an astrophysical perspective and carrying out observations in several frequencies so to obtain the best fit using a chi-squared minimization (see e.g. Simard-Normandin, Kronberg & Button 1981; Rand & Lyne 1994). This method assumed that no $n\pi$ ambiguity occurs between two closely spaced wavelengths, such that $|\Delta\varphi| < \pi/2$ is fulfilled (Ruzmaikin & Sokoloff 1979). The source is observed across a radio broad-band with sparsely sampled wavelengths, and near each observed wavelength, combinations of $(\varphi \pm n\pi)$ are considered in the fitting process. While this method can be applied to Faraday-thin media with a bright background point source, it sometimes gives multiple acceptable solutions. It does not work well for faint sources. In the Faraday-thick regime, the method will break down because the linear relation above does not hold. It is also problematic when there are multiple sources along a line of sight or when Faraday depolarization occurs (see e.g. Vallee 1980; Sokoloff et al. 1998; Farnsworth, Rudnick & Brown 2011).

Recently, alternative methods have been developed, e.g. the circular statistical method (Sarala & Jain 2001), the PACERMAN algorithm (Dolag et al. 2005; Vogt, Dolag & Enßlin 2005), the RM synthesis/RMCLEAN method (Burn 1966; Brentjens & de Bruyn 2005; Heald, Braun & Edmonds 2009), Stokes QU-fitting (e.g. Farnsworth et al. 2011; O'Sullivan et al. 2012), and the dependence on RM of neighbouring sources (Taylor, Stil & Sunstrum 2009; Ma
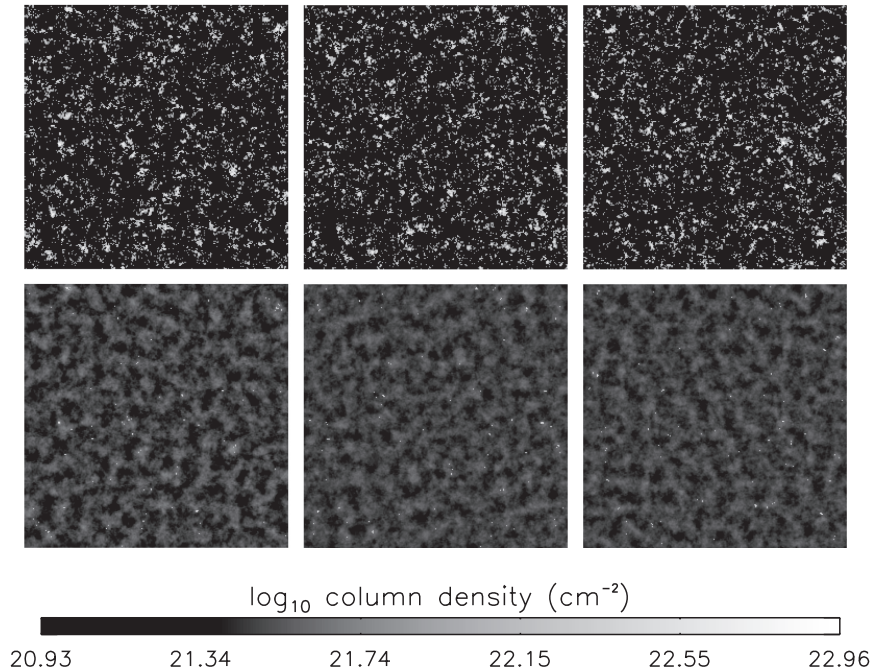
Figure 6. Column densities of Cd3 (top) and Cd5 (bottom) in the *x* (left), *y* (middle), and *z* (right) directions.
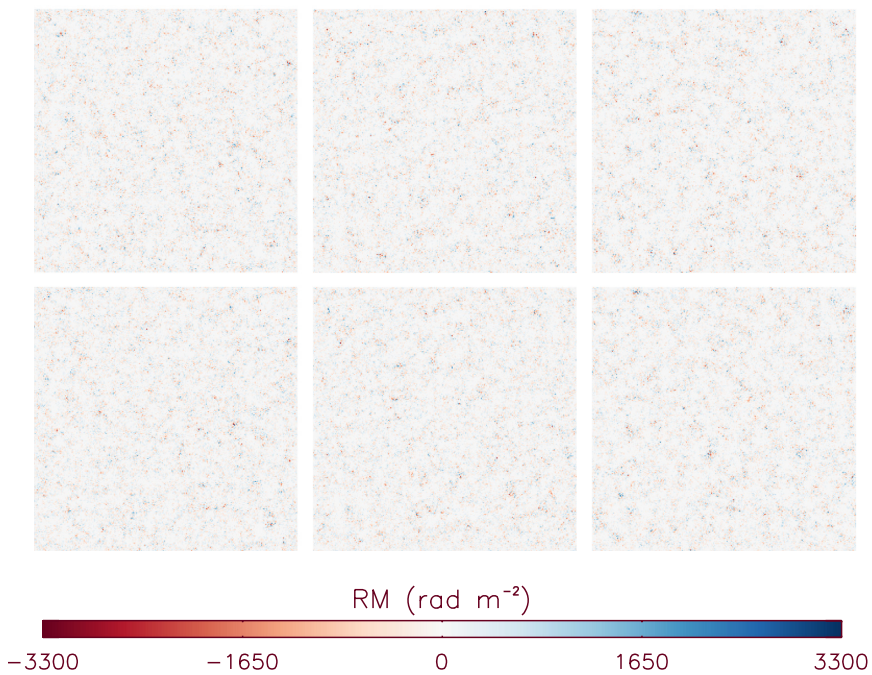
Figure 7. Synthetic RM maps of Cd2Gb (top) and Cd2Ub* (bottom) in the xy (left), xz (middle), and yz (right) planes.

et al. 2019). The $n\pi$ ambiguity is one of the obstacles that must be overcome when analysing large-scale magnetic fields using the RM information. On the other hand, we may bypass our reliance on the RM statistics by carrying out a proper (covariant) polarized radiative transfer, which can directly track the evolution of polarization along a line of sight to resolve the $n\pi$ ambiguity without having to make an a priori assumption on the Faraday complexity (see Chan et al. 2019).

4.2.2 Issues in analyses of polarization associated with large-scale astrophysical structures

FRBs and quasars as diagnostics: FRBs and quasars are exceptionally bright, polarized radio sources, observable across cosmological distances. They are therefore useful probes of the intergalactic magnetic fields (see e.g. Xu & Han 2014b; Zheng et al. 2014; Akahori et al. 2016; Ravi et al. 2016; Vazza et al. 2018; Hackstein

Table 3. The standard deviations of RM, $\sigma_\mathcal{R}^{xy}$, $\sigma_\mathcal{R}^{xz}$, and $\sigma_\mathcal{R}^{yz}$, calculated along lines of sight z, y, and x, respectively, as light travels through various configurations of magnetized, two-phase fractal plasma. The realizations are normalized to the order of magnitude typically found in galaxy clusters: $\langle n_{e,th}\rangle \sim 10^{-3}$ cm^{-3}, $B_{rms} \sim 1$ μG, and $L \sim 1$ Mpc. The magnetic fields are strictly divergence free, except for Ub*. The volume-filling factors for Cd2, Cd3, Cd4, Cd5, and Cd6 are 10^{-2}, 10^{-3}, 10^{-4}, 10^{-5}, and 10^{-6}, respectively.

Distribution		Longitudinal (equation 31)			Sky transverse (equation 32)			Ratio		
		$\sigma_\mathcal{R}^{xy}$	$\sigma_\mathcal{R}^{xz}$	$\sigma_\mathcal{R}^{yz}$	$\varsigma_\mathcal{R}^{xy}$	$\varsigma_\mathcal{R}^{xz}$	$\varsigma_\mathcal{R}^{yz}$	$\sigma^{xy}/\varsigma^{xy}$	$\sigma^{xz}/\varsigma^{xz}$	$\sigma^{yz}/\varsigma^{yz}$
Cd2	Ub*	29.2976	29.2984	29.2949	280.6983	280.0177	280.4870	0.1044	0.1046	0.1044
Cd2	Ub	29.2922	29.2979	29.3008	280.5404	279.4889	281.2761	0.1044	0.1048	0.1042
Cd2	Gb	29.2968	29.2986	29.2956	279.8605	281.7843	280.9985	0.1047	0.1040	0.1043
Cd3	Ub*	29.2976	29.2984	29.2949	471.8747	483.3400	473.8896	0.0621	0.0606	0.0618
Cd3	Ub	29.2922	29.2979	29.3008	478.3895	479.4463	476.4639	0.0612	0.0611	0.0615
Cd3	Gb	29.2968	29.2986	29.2956	466.7194	480.4994	475.2179	0.0628	0.0610	0.0617
Cd4	Ub*	29.2976	29.2984	29.2949	267.1094	271.5542	265.8259	0.1100	0.1079	0.1102
Cd4	Ub	29.2922	29.2979	29.3008	276.8559	266.4851	267.9559	0.1058	0.1099	0.1093
Cd4	Gb	29.2968	29.2986	29.2956	257.7923	271.5684	268.0812	0.1136	0.1079	0.1093
Cd5	Ub*	29.2976	29.2984	29.2949	93.4944	86.3299	89.4997	0.3134	0.3394	0.3273
Cd5	Ub	29.2922	29.2979	29.3008	98.3658	88.2455	97.2471	0.2978	0.3320	0.3013
Cd5	Gb	29.2968	29.2986	29.2956	83.6243	83.0571	89.1919	0.3503	0.3528	0.3285
Cd6	Ub*	29.2976	29.2984	29.2949	44.5203	43.3651	43.0838	0.6581	0.6756	0.6800
Cd6	Ub	29.2922	29.2979	29.3008	46.9690	43.8330	45.7565	0.6236	0.6684	0.6404
Cd6	Gb	29.2968	29.2986	29.2956	42.4488	40.6938	44.7132	0.6902	0.7200	0.6552

Table 4. The KS statistics D and p-value probabilities corresponding to the configurations in Table 3.

Distribution		D			p-value		
		xy and xz	xy and yz	xz and yz	xy and xz	xy and yz	xz and yz
Cd2	Ub*	5.7068E-03	1.9516E-02	1.9180E-02	2.3559E-01	2.7937E-11	6.5523E-11
Cd2	Ub	6.3782E-03	2.0584E-02	2.3743E-02	1.3851E-01	1.6807E-12	1.7189E-16
Cd2	Gb	4.2114E-03	1.7532E-02	2.0309E-02	6.0557E-01	3.4726E-09	3.5123E-12
Cd3	Ub*	4.5929E-03	7.0648E-03	8.1940E-03	4.9313E-01	7.5602E-02	2.4407E-02
Cd3	Ub	6.5002E-03	5.8136E-03	6.1188E-03	1.2494E-01	2.1739E-01	1.7129E-01
Cd3	Gb	3.6011E-03	8.2855E-03	7.5684E-03	7.8844E-01	2.2106E-02	4.6618E-02
Cd4	Ub*	3.1281E-03	4.2267E-03	5.7831E-03	9.0517E-01	6.0094E-01	2.2247E-01
Cd4	Ub	4.6844E-03	3.0975E-03	6.0120E-03	4.6754E-01	9.1125E-01	1.8646E-01
Cd4	Gb	3.4027E-03	6.3477E-03	6.3019E-03	8.4190E-01	1.4208E-01	1.4758E-01
Cd5	Ub*	3.0823E-03	4.3945E-03	5.8289E-03	9.1421E-01	5.5062E-01	2.1488E-01
Cd5	Ub	4.7150E-03	3.2654E-03	6.3171E-03	4.5916E-01	8.7535E-01	1.4573E-01
Cd5	Gb	3.3112E-03	6.0883E-03	5.3864E-03	8.6457E-01	1.7552E-01	2.9698E-01
Cd6	Ub*	3.0060E-03	4.5624E-03	5.9357E-03	9.2823E-01	5.0180E-01	1.9792E-01
Cd6	Ub	4.8370E-03	3.2043E-03	6.2866E-03	4.2644E-01	8.8908E-01	1.4945E-01
Cd6	Gb	3.3112E-03	5.9357E-03	5.2948E-03	8.6457E-01	1.9792E-01	3.1644E-01

et al. 2019) and their evolution (see e.g. Xu & Han 2014b), if their redshifts and dispersion measures are known (see e.g. Kronberg & Perry 1982; Blasi et al. 1999; Kronberg et al. 2008; Xu & Han 2014a; Petroff et al. 2016). Circular polarization was detected in some quasars (see e.g. Roberts et al. 1975; Saikia & Salter 1988; Rayner, Norris & Sault 2000; O'Sullivan et al. 2013) and FRBs (see e.g. Petroff et al. 2015, 2017), indicating that Faraday conversion (see e.g. Gruzinov & Levin 2019; Vedantham & Ravi 2019) or scintillation-induced variations (Macquart & Melrose 2000) might occur. As the number of detections of FRBs and quasars increases (see e.g. Keane 2018), the polarization properties of their signals can be used to better constrain large-scale magnetic field properties. Apart from the effects of Faraday conversion and scintillation, it is also important to distinguish between the RM contributions from multiple sources along the line of sight, consider the effects of traversing multiphase media, as well as taking into account of the structural evolution and stretching of radiation wavelength in an expanding Universe (see e.g. Han 2017). In these situations, RM is no longer sufficient to fully characterize the changes in polarization and hence a covariant cosmological

polarized radiative transfer treatment is necessary (see Chan et al. 2019).

Direct radio emission from large-scale structure: An emissive and Faraday-rotating medium will result in a net depolarization due to differential Faraday rotation (e.g. Sokoloff et al. 1998; Beck 1999; Shukurov & Berkhuijsen 2003; Fletcher & Shukurov 2006). This effect is particularly important in extended sources such as emitting filaments in the cosmic web. A simple Faraday screen with a bright source behind a Faraday-rotating medium would be insufficient to capture this effect properly. A covariant polarized radiative transfer calculation is therefore essential to evaluate the line-of-sight depolarization effect from all radiation processes at different redshifts (see Chan et al. 2019).

Contamination in the power spectrum: The power spectrum of the observed polarized intensity may be contaminated by emissions from the medium and embedded sources. Contributions from these sources would lead to apparent higher power in fluctuations at small scales. It is important to assess whether these signatures due to spatially separated sources can be distinguished from those imparted due to the true structures of magnetic fields. In addition
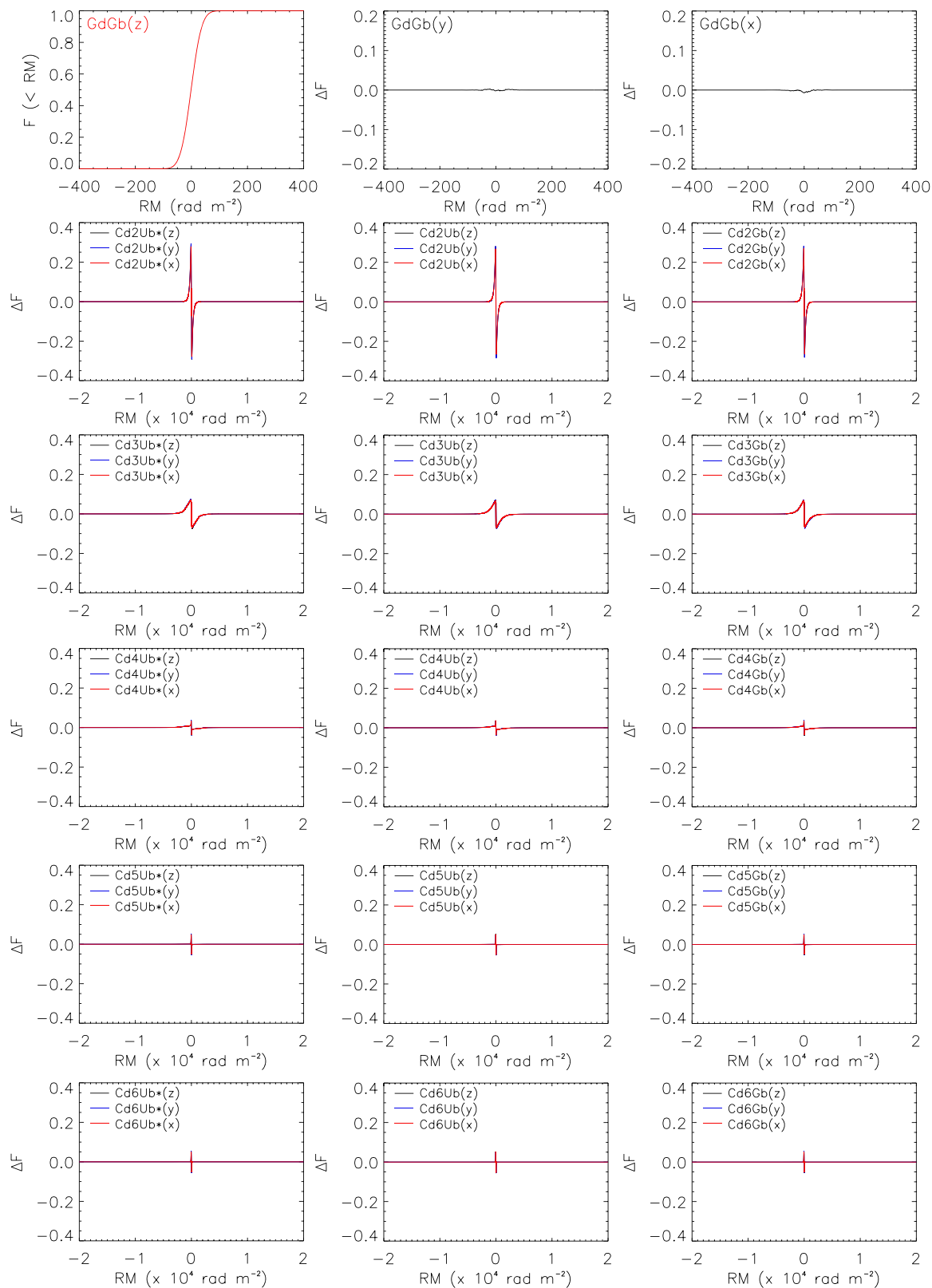
Figure 8. Top-left panel showing the CDF of GdGb(z) as a reference to calculate the numerical differences with the CDFs of GdGb(y), GdGb(x) as well as Cd2Ub*, Cd2Ub, Cd2Gb, Cd3Ub*, Cd3Ub, Cd3Gb, Cd4Ub*, Cd4Ub, Cd4Gb, Cd5Ub*, Cd5Ub, Cd5Gb, Cd6Ub*, Cd6Ub, and Cd6Gb at every line of sight.
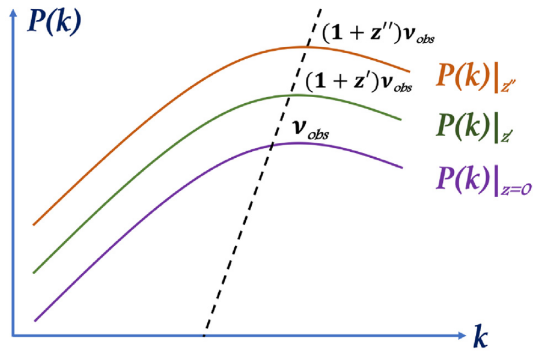
Figure 9. An illustration of how higher redshift structures can contaminate the observed power spectrum at a fixed ν_{obs} (dashed line), which differs from considering the theoretical power spectra $P(k)|_z$ from all sources at a single redshift.

to these, the interpretation of the power spectrum is complicated by the contributions at various cosmological redshifts. Consider a radio observation of the sky at a fixed frequency ν_{obs}. The observed power spectrum P_k is the result of contributions from sources at different redshifts. Hence, at each k, the power spectrum is contaminated by different levels of emission from various sources at higher redshifts (see Fig. 9), which differ from the power spectrum of the Universe at every redshift, $P(k)|_z$. Local $P(k)|_z$ does not contain any contribution from the higher redshifts, whereas observationally, different components at higher k are picked up at ν_{obs}.

5 CONCLUSIONS

Faraday RMF analysis at radio wavelengths is considered as a diagnostic tool for cosmic magnetism. Most of the current methods in RMF analyses rely on a random-walk model in which the standard deviation of RMF provides a statistical measure of the field correlation length. Our objective is to assess the validity of the conventional random-walk method as a cosmic magnetic field probe. We simulate various configurations of density and magnetic field fluctuations in astrophysical plasmas to calculate the dispersion of RM. We calculate and compare the line-of-sight longitudinal dispersion with the sky transverse dispersion.

Our results are as follows: (i) Numerically, the divergence filtering also creates a residual dipole, as a result of IDL's (Interactive Data Language) preferential direction in its Fourier transform function. This can be removed by taking a linear superposition of three orthogonal field realizations. (ii) The conventional random-walk model applies in some but not all astrophysical situations. More specifically, it is valid when the density fluctuations are uniformly distributed or Gaussian distributed. The model breaks down for densities with fractal and lognormal structures. (iii) Density fluctuations can obscure the effect of magnetic field fluctuations, and therefore affect the correlation length of magnetic fields determined by the conventional random-walk model. Our results show that it is difficult to disentangle the signals from density and field fluctuations based on the value of the standard deviation of the RM, $\sigma_{\mathcal{R}}$, itself. More specifically, our demonstration models show that different statistical indicators can potentially mislead, $\sigma_{\mathcal{R}} < \varsigma_{\mathcal{R}}$, by tens of per cents or by factors of a few (if there is unrecognized cloudiness).

Even without degeneracy between the signals from density and field fluctuations, radiative processes such as absorption and emission can confuse and ambiguate the interpretation of the

RM. Moreover, in addition to the thermal electrons, non-thermal electrons can also contribute to the Faraday rotation. We conclude that the random-walk approach is not universally valid and a more proper treatment based on (covariant) polarized radiative transfer in spatially detailed models is necessary to develop solid theoretical models and predictions in preparation for the SKA.

REFERENCES

Akahori T., Ryu D., 2010, ApJ, 723, 476
Akahori T., Gaensler B. M., Ryu D., 2014, ApJ, 790, 123
Akahori T., Ryu D., Gaensler B. M., 2016, ApJ, 824, 105
Anderson T. W., 1976, Technical Report 24, Panels and time series analysis: Markov Chains and autoregression processes. Stanford Univ., Stanford, CA
Balbus S. A., Soker N., 1989, ApJ, 341, 611
Balsara D. S., 1998, ApJS, 116, 133
Barnes D. J., Kawata D., Wu K., 2012, MNRAS, 420, 3195
Barnes D. J., On A. Y. L., Wu K., Kawata D., 2018, MNRAS, 476, 2890
Beck R., 1999, in Berkhuijsen E. M., ed., Galactic Foreground Polarization: proceedings of a workshop held in Bonn, 7-9 September 1998. Max-Planck-Institut fur Radioastronomie, Bonn, p. 3
Beck R., 2009, in Heald G., Serra P., eds, Panoramic Radio Astronomy: Wide-field 1-2 GHz Research on Galaxy Evolution, Proceedings of Science, Groningen, Netherlands, p. 46
Beck R., 2015, in Lazarian A., de Gouveia Dal Pino E. M., Melioli C., eds, Astrophysics and Space Science Library, Vol. 407, Magnetic Fields in Diffuse Media. Springer-Verlag, Berlin, p. 3
Beck R. et al., 2013, Astron. Nachr., 334, 548
Bhat P., Subramanian K., 2013, MNRAS, 429, 2469
Blasi P., Burles S., Olinto A. V., 1999, ApJ, 514, L79
Bonafede A., Feretti L., Murgia M., Govoni F., Giovannini G., Dallacasa D., Dolag K., Taylor G. B., 2010, A&A, 513, A30
Box G. E. P., Jenkins G. M., 1976, Time Series Analysis: Forecasting and Control. Holden-Day, San Francisco
Brentjens M. A., de Bruyn A. G., 2005, A&A, 441, 1217
Brown J. C., Taylor A. R., Jackel B. J., 2003, ApJS, 145, 213

Brown J. C., Haverkorn M., Gaensler B. M., Taylor A. R., Bizunok N. S., McClure-Griffiths N. M., Dickey J. M., Green A. J., 2007, ApJ, 663, 258

Burn B. J., 1966, MNRAS, 133, 67

Carilli C. L., Taylor G. B., 2002, ARA&A, 40, 319

Chan J. Y. H., Wu K., On A. Y. L., Barnes D. J., McEwen J. D., Kitching T. D., 2019, MNRAS, 484, 1427

Cho J., Ryu D., 2009, ApJ, 705, L90

Clarke T. E., 2004, J. Korean Astron. Soc., 37, 337

Combes F., 2018, in Asada K., de Gouveia dal Pino E., Nagai H., Nemmen R., Giroletti M., eds, Perseus in Sicily: from black hole to cluster outskirts, IAU-S342. Cambridge University Press, UK, p. 8

Conselice C. J., Gallagher J. S., III, Wyse R. F. G., 2001, AJ, 122, 2281

Dermer C. D., Cavadini M., Razzaque S., Finke J. D., Chiang J., Lott B., 2011, ApJ, 733, L21

Dolag K., Schindler S., Govoni F., Feretti L., 2001, A&A, 378, 777

Dolag K., Vogt C., Enßlin T. A., 2005, MNRAS, 358, 726

Elmegreen B. G., 2002, ApJ, 577, 206

Elmegreen B. G., Seiden P. E., Elmegreen D. M., 1989, ApJ, 343, 602

Farnsworth D., Rudnick L., Brown S., 2011, AJ, 141, 191

Federrath C., 2013, MNRAS, 436, 1245

Field G. B., 1965, ApJ, 142, 531

Fletcher A., Shukurov A., 2006, MNRAS, 371, L21

Ford H. C., Butcher H., 1979, ApJS, 41, 147

Fuerst S. V., Wu K., 2004, A&A, 424, 733

Gaensler B. M., Beck R., Feretti L., 2004, New Astron. Rev., 48, 1003

Gaensler B. M., Haverkorn M., Staveley-Smith L., Dickey J. M., McClure-Griffiths N. M., Dickel J. R., Wolleben M., 2005, Science, 307, 1610

Gaensler B. M., Landecker T. L., Taylor A. R., POSSUM Collaboration, 2010, in American Astronomical Society Meeting Abstracts #215, p. 515

Govoni F., Feretti L., 2004, Int. J. Mod. Phys. D, 13, 1549

Grunwald G. K., Hyndman R. J., Tedesco L. M., 1995, Technical Report, A unified view of linear AR(1) models. Department of Statistics, University of Melbourne and Department of Mathematics, Monash University, Australia

Gruzinov A., Levin Y., 2019, ApJ, 876, 74

Hackstein S., Brüggen M., Vazza F., Gaensler B. M., Heesen V., 2019, MNRAS, 488, 4220

Han J. L., 2017, ARA&A, 55, 111

Han J. L., Manchester R. N., Qiao G. J., 1999, MNRAS, 306, 371

Han J. L. et al., 2015, Proc. Sci., Three-dimensional Tomography of the Galactic and Extragalactic Magnetoionic Medium with the SKA. SISSA, Trieste, p. 41

Haverkorn M., Brown J. C., Gaensler B. M., McClure-Griffiths N. M., 2008, ApJ, 680, 362

Heald G., Braun R., Edmonds R., 2009, A&A, 503, 409

Iapichino L., Schmidt W., Niemeyer J. C., Merklein J., 2011, MNRAS, 414, 2297

Johnston-Hollitt M. et al., 2015, Proc. Sci., Using SKA Rotation Measures to Reveal the Mysteries of the Magnetised Universe. SISSA, Trieste, p. 92

Jones T. W., O'Dell S. L., 1977, ApJ, 214, 522

Katz H., Martin-Alvarez S., Devriendt J., Slyz A., Kimm T., 2019, MNRAS, 484, 2620

Keane E. F., 2018, Nature Astron., 2, 865

Kolmogorov A., 1941a, Akademiia Nauk SSSR Doklady, 30, 301

Kolmogorov A. N., 1941b, Akademiia Nauk SSSR Doklady, 32, 16

Kronberg P. P., Perry J. J., 1982, ApJ, 263, 518

Kronberg P. P., Bernet M. L., Miniati F., Lilly S. J., Short M. B., Higdon D. M., 2008, ApJ, 676, 70

Kuchar P., Enßlin T. A., 2011, A&A, 529, A13

Lee S., Lele S. K., Moin P., 1991, Phys. Fluids A, 3, 657

Macquart J. P., Melrose D. B., 2000, ApJ, 545, 798

Mao S. A., Gaensler B. M., Haverkorn M., Zweibel E. G., Madsen G. J., McClure-Griffiths N. M., Shukurov A., Kronberg P. P., 2010, ApJ, 714, 1170

Mao S. A. et al., 2017, Nature Astron., 1, 621

Marinacci F., Vogelsberger M., Mocz P., Pakmor R., 2015, MNRAS, 453, 3999

Marinacci F. et al., 2018, MNRAS, 480, 5113

Matsumoto M., Nishimura T., 1998, ACM Trans. Model. Comput. Simul., 8, 3

Ma Y. K., Mao S. A., Stil E., Basu A., West J., Heiles C., Hill A. S., Betti S. K., 2019, MNRAS, 1268

McCourt M., Sharma P., Quataert E., Parrish I. J., 2012, MNRAS, 419, 3319

McDonald M., Veilleux S., Rupke D. S. N., Mushotzky R., 2010, ApJ, 721, 1262

Miniati F., 2014, ApJ, 782, 21

Nagase F. et al., 1991, ApJ, 375, L49

Nakwacki M. S., Kowal G., Santos-Lima R., de Gouveia Dal Pino E. M., Falceta-Gonçalves D. A., 2016, MNRAS, 455, 3702

Neronov A., Vovk I., 2010, Science, 328, 73

O'Sullivan S. P. et al., 2012, MNRAS, 421, 3300

O'Sullivan S. P., McClure-Griffiths N. M., Feain I. J., Gaensler B. M., Sault R. J., 2013, MNRAS, 435, 311

Olivares V. et al., 2019, Ubiquitous cold and massive filaments in cool core clusters, submitted to A&A, preprint (arXiv:1902.09164)

Oppermann N. et al., 2012, A&A, 542, A93

Pacholczyk A. G., 1977, Radio Galaxies: Radiation Transfer, Dynamics, Stability and Evolution of a Synchrotron Plasmon. Pergamon Press, Oxford

Peacock J. A., 1999, Cosmological Physics. Cambridge Univ. Press, UK

Petroff E. et al., 2015, MNRAS, 447, 246

Petroff E. et al., 2016, Publ. Astron. Soc. Aust., 33, e045

Petroff E. et al., 2017, MNRAS, 469, 4465

Press W. H., Teukolsky S. A., Vetterling W. T., Flannery B. P., 2007, Numerical Recipes 3rd Edition: The Art of Scientific Computing, 3 edn. Cambridge Univ. Press, New York

Quataert E., 2008, ApJ, 673, 758

Rand R. J., Lyne A. G., 1994, MNRAS, 268, 497

Ravi V. et al., 2016, Science, 354, 1249

Rayner D. P., Norris R. P., Sault R. J., 2000, MNRAS, 319, 484

Reiners A., Shulyak D., Anglada-Escudé G., Jeffers S. V., Morin J., Zechmeister M., Kochukhov O., Piskunov N., 2013, A&A, 552, A103

Roberts J. A., Roger R. S., Ribes J.-C., Cooke D. J., Murray J. D., Cooper B. F. C., Biraud F., 1975, Aust. J. Phys., 28, 325

Ruzmaikin A. A., Sokoloff D. D., 1979, A&A, 78, 1

Rybicki G. B., Lightman A. P., 1979, Radiative Processes in Astrophysics. Wiley, New York

Ryu D., Schleicher D. R. G., Treumann R. A., Tsagas C. G., Widrow L. M., 2012, Space Sci. Rev., 166, 1

Saikia D. J., Salter C. J., 1988, ARA&A, 26, 93

Santangelo A. et al., 1999, ApJ, 523, L85

Sarala S., Jain P., 2001, MNRAS, 328, 623

Saxton C. J., Sutherland R. S., Bicknell G. V., 2001, ApJ, 563, 103

Saxton C. J., Bicknell G. V., Sutherland R. S., Midgley S., 2005, MNRAS, 359, 781

Schuecker P., Finoguenov A., Miniati F., Böhringer H., Briel U. G., 2004, A&A, 426, 387

Sharma P., McCourt M., Quataert E., Parrish I. J., 2012, MNRAS, 420, 3174

Shukurov A., Berkhuijsen E. M., 2003, MNRAS, 342, 496

Shu F. H., Milione V., Gebel W., Yuan C., Goldsmith D. W., Roberts W. W., 1972, ApJ, 173, 557

Simard-Normandin M., Kronberg P. P., 1980, ApJ, 242, 74

Simard-Normandin M., Kronberg P. P., Button S., 1981, ApJS, 45, 97

Sokoloff D. D., Bykov A. A., Shukurov A., Berkhuijsen E. M., Beck R., Poezd A. D., 1998, MNRAS, 299, 189

Staubert R. et al., 2019, A&A, 622, A61

Subramanian K., Shukurov A., Haugen N. E. L., 2006, MNRAS, 366, 1437

Sur S., 2019, MNRAS, 488, 3439

Takahashi K., Mori M., Ichiki K., Inoue S., Takami H., 2013, ApJ, 771, L42

Taylor A. M., Vovk I., Neronov A., 2011, A&A, 529, A144

Taylor A. R., Stil J. M., Sunstrum C., 2009, ApJ, 702, 1230

Urban O. et al., 2014, MNRAS, 437, 3939

Vacca V., Murgia M., Govoni F., Enßlin T., Oppermann N., Feretti L., Giovannini G., Loi F., 2018, Galaxies, 6, 142

Vallee J. P., 1980, A&A, 86, 251

Vazza F., Brüggen M., Hinz P. M., Wittor D., Locatelli N., Gheller C., 2018, MNRAS, 480, 3907

Vedantham H. K., Ravi V., 2019, MNRAS, 485, L78

Vernstrom T., Gaensler B. M., Rudnick L., Andernach H., 2019, ApJ, 878, 92

Vogt C., Enßlin T. A., 2003, A&A, 412, 373

Vogt C., Dolag K., Enßlin T. A., 2005, MNRAS, 358, 732

Voit G. M., Meece G., Li Y., O'Shea B. W., Bryan G. L., Donahue M., 2017, ApJ, 845, 80

Wareing C. J., Pittard J. M., Falle S. A. E. G., Van Loo S., 2016, MNRAS, 459, 1803

White T. G. et al., 2019, Nature Commun., 10, 1758

Wickramasinghe D. T., Ferrario L., 2000, PASP, 112, 873

Wickramasinghe D. T., Meggitt S. M. A., 1985, MNRAS, 214, 605

Widrow L. M., 2002, Rev. Mod. Phys., 74, 775

Widrow L. M., Ryu D., Schleicher D. R. G., Subramanian K., Tsagas C. G., Treumann R. A., 2012, Space Sci. Rev., 166, 37

Wu K., Wickramasinghe D. T., 1990, MNRAS, 246, 686

Xu J., Han J.-L., 2014a, Res. Astron. Astrophys., 14, 942

Xu J., Han J. L., 2014b, MNRAS, 442, 3329

Younsi Z., Wu K., Fuerst S. V., 2012, A&A, 545, A13

Zheng Z., Ofek E. O., Kulkarni S. R., Neill J. D., Juric M., 2014, ApJ, 797, 71

APPENDIX A: DIVERGENCE-FREE FILTER FOR THE MAGNETIC FIELD

Consider a vector $\boldsymbol{k}\,(=k_i)$, defining a reference axis in a vector space. Any other arbitrary vector $\boldsymbol{X}$ can be decomposed into two components, one parallel to and another one perpendicular to $\boldsymbol{k}$: $\boldsymbol{X} = \boldsymbol{X}_\parallel^{(k)} + \boldsymbol{X}_\perp^{(k)}$, with $\left| \boldsymbol{k} \cdot \boldsymbol{X}_\parallel^{(k)} \right| \geq 0$ and $\boldsymbol{k} \cdot \boldsymbol{X}_\perp^{(k)} = 0$. Now introduce a projection operator $\mathcal{P}(\boldsymbol{k})$, such that $\boldsymbol{X}' = \mathcal{P}(\boldsymbol{k})\,\boldsymbol{X} = \boldsymbol{X}_\perp^{(k)}$. This projection operator eliminates the longitudinal component of $\boldsymbol{X}$, ensuring that $\boldsymbol{k} \cdot \boldsymbol{X}' = 0$ for any given $\boldsymbol{X}$. A non-trivial example of $\mathcal{P}(\boldsymbol{k})$ is $(\boldsymbol{I} - \hat{\boldsymbol{k}}\hat{\boldsymbol{k}})$, where $\boldsymbol{I}$ is an identity operator and $\hat{\boldsymbol{k}} = \boldsymbol{k}/|\boldsymbol{k}|$, such that

$$\boldsymbol{k} \cdot \left[\left(\boldsymbol{I} - \hat{\boldsymbol{k}}\hat{\boldsymbol{k}} \right) \cdot \boldsymbol{X} \right] = k_i \left(\delta_{ij} - \frac{k_i k_j}{k^2} \right) X_j = 0. \tag{A1}$$

Magnetic fields in vacuum are solenoidal, i.e. divergence-free, satisfying $\nabla \cdot \boldsymbol{B} = \partial_i B_i = 0$. In Fourier space, the divergence-free relation is expressed as $\boldsymbol{k} \cdot \boldsymbol{B}(\boldsymbol{k}) = k_i B_i = 0$, which requires that the field component parallel to $\boldsymbol{k}$ must vanish. Thus, we may apply the filter $(\boldsymbol{I} - \hat{\boldsymbol{k}}\hat{\boldsymbol{k}})$ in Fourier space to prepare a divergence-free magnetic field (with designated structural properties) from a generic initial simulated random vector field (with otherwise the same structural properties). The procedures are as follows:

(i) Construct a random field $\tilde{\boldsymbol{B}}(\boldsymbol{k})\,(= \tilde{B}_i(k_m))$ according to the specified structural properties in Fourier space.

(ii) Apply the divergence-free filter, i.e. carry out the projection operation: $B_i(k_m) = (\delta_{ij} - k_i k_j/k^2)\tilde{B}_j(k_m)$.

(iii) Use an inverse-Fourier transform on $B_i(k_m)$ to obtain $B_i(x_m)$ in configuration space.

As the filtering process removes the longitudinal part of the magnetic field in Fourier space, it reduces the total magnetic energy stored in the system. The Parseval's (energy) theorem,

$$\int_{V_x} \mathrm{d}^3\boldsymbol{x} \left| \boldsymbol{B}(\boldsymbol{x}) \right|^2 = \int_{V_k} \mathrm{d}^3\boldsymbol{k} \left| \boldsymbol{B}(\boldsymbol{k}) \right|^2, \tag{A2}$$

requires that the total magnetic energy is reduced by the same amount in configuration space as in Fourier space. With the divergence-free magnetic field given by $\boldsymbol{B}(\boldsymbol{k}) = (\boldsymbol{I} - \hat{\boldsymbol{k}}\hat{\boldsymbol{k}})\,\tilde{\boldsymbol{B}}(\boldsymbol{k})$, the energy density of the magnetic field is

$$\frac{1}{8\pi} \left| \boldsymbol{B} \right|^2 = \frac{1}{8\pi} \left[\left(\delta_{ij} - \frac{k_i k_j}{k^2} \right) \left(\delta_{im} - \frac{k_i k_m}{k^2} \right) \tilde{B}_j \tilde{B}_m \right]$$

$$= \frac{1}{8\pi} \left[\tilde{B}_i \tilde{B}_i - \frac{1}{k^2} \left(k_i \tilde{B}_i \right)^2 \right]$$

$$= \frac{1}{8\pi} \left| \tilde{\boldsymbol{B}} \right|^2 \left(1 - \mu^2 \right), \tag{A3}$$

where $\mu = \hat{\boldsymbol{k}} \cdot \tilde{\boldsymbol{B}}/|\tilde{\boldsymbol{B}}|$. For a randomly oriented magnetic field in Fourier space,

$$\left\langle 1 - \mu^2 \right\rangle = \frac{1}{2} \int_{-1}^{1} \mathrm{d}\mu \, \left(1 - \mu^2 \right) = \frac{2}{3}. \tag{A4}$$

Hence, one-third of the magnetic energy density is filtered out. This is the expected amount when there is equipartition between the energies in the longitudinal component and the two orthogonal perpendicular components (the solenoidal components) of the initial 'magnetic' field $\tilde{\boldsymbol{B}}$. To recover the energy loss in the divergence-free filtering process, we may renormalize the resulting divergence-free magnetic field, either in configuration space or in Fourier space, by a multiplicative factor $\sqrt{3/2}$.

APPENDIX B: PREPARATION OF THE MODEL TWO-PHASE FRACTAL CLOUDS

Starting from even the most minute inhomogeneities, astrophysical plasmas are susceptible to form substructures through a variety of thermal, magnetic, and buoyancy instabilities (e.g. Field 1965; Shu et al. 1972; Balbus & Soker 1989; Quataert 2008; McCourt et al. 2012; Sharma et al. 2012; Wareing et al. 2016). An optically thin plasma of nearly solar composition has a temperature-dependent radiative cooling function that incurs thermal instability over an interval $10^4\,\mathrm{K} \lesssim T \lesssim 10^7\,\mathrm{K}$. An initially homogeneous medium can spontaneously self-segregate into a quasi-equilibrium of two coexisting phases: the original hot diffuse medium and a minor component of cooler dense clouds. Externally imposed isobaric conditions imply a density ratio $\gtrsim 10^3$ between the phases, in the absence of any further gravitational collapse. Thermally condensed clouds are endemic in otherwise hot extragalactic media, and can stretch into filaments in upflows and downflows associated with active galaxies (e.g. Ford & Butcher 1979; Conselice et al. 2001; Saxton, Sutherland & Bicknell 2001; McDonald et al. 2010; Voit et al. 2017; Combes 2018; Olivares et al. 2019).

As a test of RMF due to strong density inhomogeneities, we build two-phase toy models capable of approximating the knotty medium of a galaxy cluster core, or the ISM of an elliptical galaxy that acquired clouds (either via thermal instability or a wet–dry merger). Initially we generate a Gaussian distribution of pseudo-random complex numbers, and apply an amplitude filter to obtain a Kolmogorov-like power spectrum. This cube is transformed according to the Elmegreen recipe for imitating lognormal density fluctuations in a turbulent medium, which will represent the diffuse phase. We prescribe a volume-filling factor of clouds $(0 < f \ll 1)$ and select the densest-ranked voxels, down to a suitable threshold. Their densities are multiplied by a uniform constant, set to ensure a mean density ratio of 10^3 between the cloud and non-cloud phases. Assuming that the clouds are condensing from the hot medium, we normalize the mean of the entire cloudy block to

Table B1. Summary of cloudy model properties: volume-filling factors f; cloud mass fraction, area covering factors for the three orthogonal views. Before radiative transfer calculations, all models are normalized to the same total mass or mean density.

Model	$\log f$	m_c/M	a_x/A	a_y/A	a_z/A
Cd2	−2.01	0.912	0.713	0.752	0.749
Cd3	−3.01	0.495	0.150	0.155	0.155
Cd4	−4.02	0.0877	0.0188	0.0190	0.0189
Cd5	−5.12	0.00746	0.00171	0.00172	0.00169
Cd6	−6.32	0.000477	0.000122	0.000122	0.000122

10^{-3} cm^{-3}, matching the standard for our single-phase density models.

We create and test models ranging from a negligible smattering of clouds ($f \approx 10^{-6}$) to a heavily obscured overcast case ($f \approx 10^{-2}$) where a majority ($\gtrsim 0.7$) of RM map pixels or rays traverse at least one dense cloud. Table B1 presents basic global properties of these models. In area terms, the cloud coverage factors decrease with f, and vary with orientation due to the clouds' random fractal shapes. Clouds account for only a tiny fraction of the total mass in Cd4–Cd6, or just under half the mass in Cd3. The overcast case Cd2 is dominated by the mass of the dense cold phase, making it unrealistic for the filament-infused core of a galaxy cluster (where the cold fraction is at most a few tens of per cents), but perhaps more like the primordial medium of a hypothetical wet protogalaxy. The mean densities of the cubes vary by factors of a few before their normalizations into fiducial ICM units.

This paper has been typeset from a TeX/LaTeX file prepared by the author.